

The vertical structure and entrainment of subglacial melt water plumes

Hans Burchard¹, Karsten Bolding², Adrian Jenkins^{3,4}, Martin Losch⁵, Markus Reinert¹, and Lars Umlauf¹

¹Leibniz Institute for Baltic Sea Research Warnemünde, Seestr. 15, D-18119 Rostock, Germany

²Bolding & Bruggeman ApS., Strandgyden 25, DK-5466 Asperup, Denmark

³British Antarctic Survey, Natural Environment Research Council, Cambridge, United Kingdom

⁴Department of Geography and Environmental Sciences, Northumbria University, Newcastle upon Tyne, United Kingdom

⁵Alfred-Wegener-Institut, Helmholtz-Zentrum für Polar- und Meeresforschung, Bremerhaven, Germany

Key Points:

- A vertically resolving model with second-moment turbulence closure has been constructed for subglacial plumes
- Convergent numerical formulations for the ocean-to-ice fluxes of momentum, fresh-water and heat have been derived from an analytical model
- Model results are consistent with bulk parameterizations for the entrainment of ambient water

Corresponding author: Hans Burchard, hans.burchard@io-warnemuende.de

Abstract

Basal melting of marine-terminating glaciers, through its impact on the forces that control the flow of the glaciers, is one of the major factors determining sea level rise in a world of global warming. Detailed quantitative understanding of dynamic and thermodynamic processes in melt-water plumes underneath the ice-ocean interface is essential for calculating the subglacial melt rate. The aim of this study is therefore to develop a numerical model of high spatial and process resolution to consistently reproduce the transports of heat and salt from the ambient water across the plume into the glacial ice. Based on boundary layer relations for momentum and tracers, stationary analytical solutions for the vertical structure of subglacial non-rotational plumes are derived, including entrainment at the plume base. These solutions are used to develop and test convergent numerical formulations for the momentum and tracer fluxes across the ice-ocean interface. After implementation of these formulations into a water-column model coupled to a second-moment turbulence closure model, simulations of a transient rotational subglacial plume are performed. The simulated entrainment rate of ambient water entering the plume at its base is compared to existing entrainment parameterizations based on bulk properties of the plume. A sensitivity study with variations of interfacial slope, interfacial roughness and ambient water temperature reveals substantial performance differences between these bulk formulations. An existing entrainment parameterization based on the Froude number and the Ekman number proves to have the highest predictive skill. Recalibration to subglacial plumes using a variable drag coefficient further improves its performance.

Plain Language Summary

In a world of global warming, the melting of glaciers terminating as floating ice tongues into the oceans of Arctic and Antarctic regions allows those glaciers to flow faster and hence to make a considerable contribution to global mean sea-level rise. Underneath the ice-ocean interface, turbulent currents of the order of 10 m thickness (so-called plumes) develop that transport the melt water from the grounding line where the glacier enters the ocean towards the calving front that marks the seaward end of the glacier. At its base, ambient relatively warm and salty ocean water is mixed into the plumes and is vertically transported towards the ice-ocean interface, where the melting is increased due to the additional heat supply. Understanding these processes is essential for their incorporation into computer simulation models for the prediction of such melt processes. In the present study, an accurate simulation model for the water column (vertical direction only) is constructed that is able to consistently reproduce these processes. The algorithms developed here are proven to provide reliable results also for relatively coarse vertical resolution and can therefore be implemented into climate models to more accurately simulate future scenarios of sea level rise.

1 Introduction

The accelerated melting of Greenland's glaciers contributed to a net global mean sea level rise of 7.5 mm during the years 1992-2011 (Church et al., 2011). Around Greenland, the melt water enters the ocean largely through glacial fjords, mainly as subglacial discharge at the grounding lines of marine-terminating glaciers or as subglacial melt fluxes at the ice-ocean interface (Straneo & Cenedese, 2015). Increased melting at the ice-ocean interface it thought to be responsible for the acceleration of many of Greenland's marine terminating glaciers and thus to have contributed to the sea level rise. Some large Greenland fjords are covered with ice tongues of marine-terminating glaciers such as the Nioghalvfjærdsfjorden, also called 79°N glacier fjord (Mayer et al., 2018), and the Petermann Gletscher (Münchow et al., 2014). For these glaciers the link between submarine

67 melting and glacier flow is clear, because melt-driven thinning of the floating ice tongue
68 reduces buttressing of the flow across the grounding line (Goldberg et al., 2009).

69 For the largest floating ice tongue of the 79°N glacier, only 11% of the freshwater
70 enters the fjord directly as subglacial discharge, and about 89% stems from subglacial
71 melting at the ice-ocean interface (Schaffer et al., 2020). Hence, a cold and relatively fresh
72 buoyant water mass composed of contributions from subglacial discharge, melt water and
73 entrained ambient ocean water is produced that propagates upwards towards the calving
74 front as a turbulent plume (Hewitt, 2020). The correct quantification and predic-
75 tion of the subglacial melt rate under highly variable environmental conditions has been
76 an aim of polar oceanography for decades. Melt processes in the melt layer are typically
77 parameterized based on a three-equation model for melt-layer temperature, melt-layer
78 salinity and melt rate derived from equilibrium fluxes of freshwater and heat across the
79 melt layer (Hellmer & Olbers, 1989). The challenge is to relate these processes to the
80 properties of the underlying subglacial plume. To this end, similarity relations are typ-
81 ically applied, resulting in logarithmic profiles for momentum and tracers in the near-
82 interfacial region of the melt water plume (Kader & Yaglom, 1972; Yaglom & Kader, 1974;
83 Kader, 1981).

84 After applying the similarity relations for a vertically integrated model of subglacial
85 plumes (Jenkins, 1991, 1992), plume models have become powerful tools for understand-
86 ing melt processes underneath floating ice tongues and ice shelves (P. R. Holland & Feltham,
87 2006; Payne et al., 2007; Jenkins et al., 2010; Jenkins, 2011). Their strength is the com-
88 putational efficiency allowing high horizontal resolution and the reproduction of the plume
89 thickness, but they rely on accurate parameterizations of entrainment of ambient ocean
90 water into the plume. Many different entrainment parameterizations exist (Jungclaus
91 & Backhaus, 1994; Arneborg et al., 2007; Wells et al., 2010). These are generally derived
92 for dense bottom currents and typically depend on non-dimensional bulk parameters such
93 as the bulk Richardson number, the Froude number or the Ekman number. A specifi-
94 cally simple and robust parameterization is based on a constant entrainment rate (ratio
95 of entrainment velocity to plume current speed, Jenkins, 1991). The diversity of entrain-
96 ment parameterizations shows that there is quite an uncertainty in determining the plume
97 dynamics. In spite of their success, plume models have their specific limitations: They
98 do not predict the ocean temperature and salinity underneath the plume such that the
99 amount of entrained heat and salt is highly uncertain.

100 To overcome the limitations of plume models and to predict better the effects of
101 larger scale ocean processes, three-dimensional ocean models with explicit ice shelf-ocean
102 interfaces were developed.

103 For ocean models with geopotential coordinates, a result of the typical step-like ap-
104 proximation of slopes is that the sloping ice-ocean interface is poorly resolved (Losch,
105 2008). To avoid this issue, terrain-following coordinates are often used where the top layer
106 follows the ice-ocean interface and the lower most layer follows the bottom topography,
107 with non-linear zooming of layers towards surface and bottom (Dinniman et al., 2007).
108 Due to the pressure gradient errors in models with terrain-following coordinates (Haney,
109 1991), large scale ocean models including ice shelves sometimes apply hybrid coordinates
110 with terrain-following properties inside ice shelves and geopotential coordinates elsewhere
111 (Timmermann et al., 2012). Terrain-following coordinates have the clear advantage of
112 smoothly resolving the ice-ocean interface at high vertical resolution. However, their dis-
113 advantage is that the vertical resolution near the ice-ocean interface depends directly on
114 the water depth. Typical top-layer resolutions of terrain-following ice-shelf models around
115 Antarctica vary between 0.5 m near the grounding line and 5 m near the calving front
116 (Gwyther et al., 2020). In models with higher vertical resolution near the ice-ocean in-
117 terface, the insulating effect of subglacial plumes could be better reproduced than coarse-
118 resolution models (Gwyther et al., 2020). As a consequence, coarse resolution models
119 tend to overestimate melt rates at the ice-ocean interface. Vertically adaptive coordi-

120 nates with specifically high resolution in the entrainment layer (Hofmeister et al., 2010;
 121 Gräwe et al., 2015), which would have the potential to resolve subglacial plumes inde-
 122 pendently of the water depth, have not yet been used in models with an ice shelf-ocean
 123 interface.

124 We can expect that improved strategies for vertical coordinates and available com-
 125 puter resources will allow very high vertical resolution of subglacial plumes and grav-
 126 ity currents, so that related processes can be simulated more accurately with the prospect
 127 of higher predictability of the melt rate. A similar emphasis should be placed on real-
 128 istic turbulence closure schemes in circulation models underneath ice shelves, because
 129 the basal melt rates strongly depend on the parameterization of mixing processes and
 130 entrainment (Dansereau et al., 2014). Exploring these aspects is best to be done with
 131 one-dimensional water-column models, because with these, very high vertical resolution
 132 can be achieved at little computational cost.

133 Water column models, also with second-moment turbulence closures, have been used
 134 to study melting (and freezing) under sea ice (Omstedt & Svensson, 1984; Mellor et al.,
 135 1986; Steele et al., 1989). Analogous studies of the vertical structure of subglacial plumes
 136 are in their infancy, but include models with simple (Jenkins, 2016, 2021) and two-equation
 137 turbulence closures (C. Cheng et al., 2020). In these models, a well-mixed turbulent bound-
 138 ary layer is separated from the ambient water underneath by a stratified layer at marginal
 139 stability, across which quiescent ambient water is entrained. The resulting profiles of ve-
 140 locity and eddy diffusivity are very sensitive to parameters such as the roughness of the
 141 ice-ocean interface or the transfer velocities for salt and heat. However, the simplicity
 142 of the applied turbulence closures in the former case and the particularity of the appli-
 143 cation in the latter case render general applicability of the results very uncertain specifi-
 144 cally in the region of the entrainment layer. While Direct Numerical Simulation (DNS,
 145 Rosevear et al., 2021) and Large Eddy Simulation (LES, Vreugdenhil & Taylor, 2019)
 146 have been applied to the ice-shelf-ocean boundary, the entrainment layer has not yet been
 147 studied in these applications because of the limited spatial scales considered. In the present
 148 study we overcome these limitations and develop, present, and apply a more general high-
 149 resolution water-column model for subglacial plumes that includes realistic second-moment
 150 turbulence closures.

151 Melt processes under floating ice tongues are very difficult to observe in their harsh
 152 and barely accessible polar environments. Therefore, the dynamic analogy between buoy-
 153 ant plumes under shelf ice and dense bottom currents due to overflows across sills have
 154 been applied to validate plume models (Jenkins, 2016). The main difference is that in
 155 ice shelves the buoyancy is mostly produced locally due to subglacial melt, but the (neg-
 156 ative) buoyancy in dense bottom currents is a result of upstream processes. While this
 157 certainly has substantial effects on larger time and space scales, the vertical structure
 158 of both regimes may be comparable. Exploiting this analogy, most formulations for en-
 159 trainment in plume models are derived from studies of dense bottom currents. In the
 160 present study, we apply previous modeling concepts of simulating rotational dense bot-
 161 tom currents in the Western Baltic Sea (Arneborg et al., 2007; Umlauf et al., 2010). The
 162 subglacial plume model developed here serves the following purposes:

- 163 1. develop a consistent dynamic coupling between parameterized melt layer processes
 164 and turbulent processes within the plume and the entrainment layer,
- 165 2. develop consistent and convergent discretization methods for melt fluxes that give
 166 robust results also for relatively coarse resolution, and
- 167 3. test existing formulations and calibrate a new parameterization of entrainment that
 168 can be applied in vertically integrated plume models.

169 This paper is structured as follows: First, the underlying mathematical formula-
 170 tions are given, with the water-column equations (Sec. 2.1), the boundary conditions (Sec.

171 2.2), the melt formulations (Sec. 2.3), the tracer roughness lengths (Sec. 2.4), and a sta-
 172 tionary analytical model of the vertical plume structure (Sec. 2.5). Afterwards, numer-
 173 ical issues are discussed, with discretization methods for velocity (Sec. 3.1) and tracers
 174 (Sec. 3.2), the numerical treatment of the free surface (Sec. 3.3), and with numerical con-
 175 vergence experiments (Sec. 3.4). The transient model simulations with the turbulence
 176 closure model are described, with the model setup (Sec. 4.1), the models results includ-
 177 ing the default scenario and sensitivity studies are presented (Sec. 4.2), and a compar-
 178 ison of the model results to the performance of entrainment parameterizations is made,
 179 including calibration of a new formulation (Sec. 4.3). Finally, the main results of the study
 180 are discussed (Sec. 5) and some conclusions are drawn (Sec. 6). In the appendix, details
 181 of the analytical solution (Sec. Appendix A) and an analytical dependence of plume speed
 182 and friction velocity on the interfacial roughness length (Sec. Appendix B) are given.

183 2 Materials and Methods

184 2.1 Water-column model equations

185 The hydrodynamic and hydrographic water column equations for a buoyant melt
 186 water plume under a planar ice-ocean interface with slope $\partial_x z_b = \tan \alpha_x$, $\partial_y z_b = \tan \alpha_y$
 187 (with the vertical position of the ice-ocean interface $z = z_b$, where z is the upward di-
 188 rected vertical coordinate with the origin at the undisturbed mean sea level) are based
 189 on the Reynolds-averaged Navier-Stokes equations with the Boussinesq assumption and
 190 the down-gradient parameterization of vertical turbulent fluxes (Umlauf & Burchard, 2005).
 191 We assume that stagnant and homogeneous ambient water with velocities $u = v = 0$,
 192 potential temperature $\theta = \theta_0$, salinity $S = S_0$ and potential density $\rho = \rho_0$ below the
 193 plume. The z -axis is assumed to be pointing upwards exactly opposite to the gravita-
 194 tional acceleration. The plume properties are assumed to be homogeneous along the ice-
 195 ocean interface, i.e. all gradients along the slope vanish:

$$196 \quad \partial_x = -\tan \alpha_x \cdot \partial_z, \quad \partial_y = -\tan \alpha_y \cdot \partial_z. \quad (1)$$

197 In a one-dimensional hydrostatic water column model the pressure-gradient driven ac-
 198 celeration in x -direction is calculated as

$$199 \quad -\frac{1}{\rho_0} \partial_x p = -\frac{1}{\rho_0} \partial_x p(z_b) - \frac{g}{\rho_0} \rho(z_b) \tan \alpha_x - \frac{g}{\rho_0} \int_z^{z_b} \partial_x \rho dz', \quad (2)$$

200 with the surface pressure $p(z_b)$ (from atmospheric pressure plus the additional pressure
 201 due to glacial ice). Using (1) we obtain

$$202 \quad -\frac{1}{\rho_0} \partial_x p = -\frac{1}{\rho_0} \partial_x p(z_b) - \frac{g}{\rho_0} \rho \tan \alpha_x. \quad (3)$$

203 For the ambient stagnant water below the plume with $z \rightarrow -\infty$ and $\rho(-\infty) = \rho_0$, we
 204 demand that the pressure gradient vanishes, i.e.,

$$205 \quad 0 = -\frac{1}{\rho_0} \partial_x p(z_b) - \frac{g}{\rho_0} \rho_0 \tan \alpha_x, \quad (4)$$

206 such that we obtain

$$207 \quad -\frac{1}{\rho_0} \partial_x p = -\frac{g}{\rho_0} (\rho - \rho_0) \tan \alpha_x = b \tan \alpha_x \quad (5)$$

208 with the buoyancy

$$209 \quad b = -g \frac{\rho - \rho_0}{\rho_0}, \quad (6)$$

210 which is positive inside the subglacial plume and vanishes in the ambient water. The pres-
 211 sure gradient in y -direction is calculated accordingly, such that the dynamic equations
 212 for the velocity components u and v read

$$213 \quad \partial_t u - \partial_z (\nu_t \partial_z u) - f v = b \tan \alpha_x, \quad (7)$$

$$\partial_t v - \partial_z (\nu_t \partial_z v) + f u = b \tan \alpha_y,$$

214 with the eddy viscosity ν_t and the Coriolis frequency f . The second terms on the left
 215 hand side represents the stress divergence with the stress vector

$$216 \quad (\tau^x, \tau^y) = \rho_0 \nu_t (\partial_z u, \partial_z v). \quad (8)$$

217 Similar dynamic equations have been used for simulations of subglacial plumes (Jenkins,
 218 2016, 2021) as well as for dense bottom currents, where less dense ambient water resides
 219 above the plume (Arneborg et al., 2007). In both modelling concepts, the coordinate sys-
 220 tem is defined such that the z -axis is orthogonal to the slope of the model instead of be-
 221 ing aligned with the gravitational forcing. However, for mild slopes, the differences to
 222 our approach outlined above are negligibly small. In the present study, the formulation
 223 of a vertical z -axis is used in order to be consistent with hydrostatic three-dimensional
 224 ocean models, which loose their validity for steep slopes where the vertical acceleration
 225 becomes relevant.

226 The budget equations for potential temperature θ and salinity S are formulated
 227 as

$$228 \quad \begin{aligned} \partial_t \theta - \partial_z (\nu_t' \partial_z \theta) &= 0, \\ \partial_t S - \partial_z (\nu_t' \partial_z S) &= 0, \end{aligned} \quad (9)$$

229 with the eddy diffusivity ν_t' . The hydrographic equations (9) are linked to the hydrody-
 230 namic equations (7) by means of an equation of state for potential density,

$$231 \quad \rho = \rho(\theta, S, p_0), \quad (10)$$

232 calculated according to Jackett et al. (2006), with the atmospheric pressure at the sea
 233 surface, p_0 . Consequently, $\rho_0 = \rho(\theta_0, S_0, p_0)$. Water column stability at a depth with
 234 pressure $p_z = \text{const}$, i.e. $\partial_z p_z = 0$, is then calculated as

$$235 \quad N^2 = \partial_z b = -\frac{g}{\rho_0} \dot{\rho}(\theta, S, p_z) = \partial_\theta \rho(\theta, S, p_z) \partial_z \theta + \partial_S \rho(\theta, S, p_z) \partial_z S, \quad (11)$$

236 with the Brunt-Väisälä frequency N .

237 Eddy viscosity ν_t and eddy diffusivity ν_t' are calculated in two ways here. For the
 238 analytical calculations presented in Sec. 2.5, 2.5.3, 3 and Appendix A parabolic profiles
 239 for ν_t and ν_t' are chosen that extend over the entire thickness of the plume, see Sec. A1
 240 and A2. Such parabolic profiles are often used for well-mixed open channel flow, see the
 241 recent discussion by Absi (2021) and allow for analytical treatment of velocity and tracer
 242 profiles (Burchard et al., 2013; Lange & Burchard, 2019).

243 For more realistic simulations that do also allow for predictions of entrainment rates
 244 at the base of the plumes, eddy viscosity and eddy diffusivity are determined by means
 245 of a two-equation turbulence closure model with an algebraic second-moment closure (Umlauf
 246 & Burchard, 2005). This closure is based on an equilibrium assumption for the second
 247 moments (turbulent transports of momentum and tracers), that is, the transport terms
 248 for the second moments are neglected and only the source and sink terms are retained.
 249 The two equations of the closure model represent budgets of the turbulent kinetic en-
 250 ergy k and its dissipation rate ε . The eddy coefficients are then calculated as

$$251 \quad \nu_t = c_\mu (\alpha_N) \frac{k^2}{\varepsilon}, \quad \nu_t' = c'_\mu (\alpha_N) \frac{k^2}{\varepsilon}, \quad (12)$$

252 where c_μ and c'_μ are quasi-equilibrium (assuming an equilibrium condition for the bud-
 253 get of k only for the second-moment closure) non-dimensional stability functions repre-
 254 senting the second-moment closure. The argument of the stability functions is the non-
 255 dimensional buoyancy number

$$256 \quad \alpha_N = \frac{N^2 k^2}{\varepsilon^2}. \quad (13)$$

The weak-equilibrium stability functions that additionally depend on a non-dimensional shear number (Umlauf & Burchard, 2005) are not used since they were found to induce some small-scale oscillations in the entrainment layer at the base of the subglacial plume.

The buoyancy term in the ε equation is calibrated in a way that for homogeneous shear layers in equilibrium the gradient Richardson number converges towards the steady-state value of one quarter (Burchard & Baumert, 1995). This guarantees the correct representation of entrainment rates at the base of surface mixed layers (Umlauf & Burchard, 2005) or on top of dense bottom currents (Umlauf et al., 2010).

In contrast to the second-moment closure used here, C. Cheng et al. (2020) applied the approach of a standard- k - ε model with constant stability functions for their simulations of super-cooled subglacial plumes. In their model, the buoyancy term is not specifically calibrated for reproduction of realistic entrainment rates.

2.2 Boundary conditions

At the upper boundary at $z = z_b$ (ice-ocean interface) a no-slip boundary condition for velocity is fulfilled:

$$u = 0, \quad v = 0, \quad \text{for } z = z_b. \quad (14)$$

The velocity no-slip boundary conditions in (14) are equivalent to the flux boundary conditions

$$-\nu_t \partial_z u = \frac{\tau^{b,x}}{\rho_0} = u_*^{b,x} u_*^b, \quad -\nu_t \partial_z v = \frac{\tau^{b,y}}{\rho_0} = u_*^{b,y} u_*^b, \quad \text{for } z = z_b, \quad (15)$$

with the interfacial shear stress vector $(\tau^{b,x}, \tau^{b,y})$, its absolute value $\tau^b = (u_*^b)^2 \rho_0$ and the interfacial friction velocity $u_*^b = \sqrt{(u_*^{b,x})^2 + (u_*^{b,y})^2}$.

In the framework of this water-column model, the upper boundary is treated as a rigid lid, i.e. melt and freezing processes do not lead to a change in water depth, other than in free-surface models. The dilution of the surface water due to addition of melt water is parameterized here as a virtual salinity flux, see Jenkins et al. (2001) for a discussion of boundary conditions for material (rigid-lid) and immaterial (free-surface) boundary treatment at the ice-ocean interface. Free-surface boundary conditions for freshwater and heat, where the melt water is added to the water column, are given in Sec. 2.3. The diffusive ocean-to-ice fluxes (orthogonal to the ice-ocean interface) of potential temperature and salinity, f_b^T and f_b^S , are located at the same position as the no-slip condition for momentum:

$$-\nu_t' \partial_z \theta = f_b^T, \quad -\nu_t' \partial_z S = f_b^S, \quad \text{for } z = z_b. \quad (16)$$

Note that $Q_M^T = c \rho_0 f_b^T$ is the ocean-to-ice heat flux at the ice-ocean interface, with the heat capacity of ocean water, c . For simplicity, we apply the ocean-to-ice fluxes in the vertical direction, without prior projection from the orthogonal direction. This approximation is valid for small slopes. For example, for a slope of $\tan \alpha_x = 5 \cdot 10^{-3}$ (i.e., a slope angle of 0.28°), the error is about $5 \cdot 10^{-3}$.

Near the boundary, the spatial variation of all momentum and tracer fluxes can be neglected, such that their exact vertical location within the melt layer is not relevant. This plays a role when constructing logarithmic near-boundary profiles based on these fluxes and Dirichlet boundary conditions that are located at slightly different vertical locations (see Sec. 2.4).

The boundary conditions for the turbulent quantities at the ice-ocean interface are best explained by means of near-boundary profiles as functions of the distance from the

interface, $z' = z_b - z$:

$$k(z') = \frac{(u_*^b)^2}{(c_\mu^0)^{1/2}}, \quad \varepsilon(z') = \frac{(u_*^b)^3}{\kappa(z' + z_0)}, \quad (17)$$

where c_μ^0 is the equilibrium stability function for unstratified conditions, κ is the van Karman constant, and z_0 is the hydrodynamic roughness of the ice-ocean interface (see Sec. 2.4 for details). From the turbulence boundary profiles (17) two sets of boundary conditions for $z' = 0$ have been derived, Dirichlet conditions and Neumann conditions, of which Burchard and Petersen (1999) could show that the latter are much more accurate. Note that with (12), the near-interface profile of the eddy viscosity is linear:

$$\nu_t = \kappa u_*^b (z' + z_0). \quad (18)$$

Far away in the ambient and stagnant water with $z \rightarrow -\infty$, the boundary conditions are

$$u = 0, \quad v = 0, \quad \theta = \theta_0, \quad S = S_0, \quad \partial_z k = 0, \quad \partial_z \varepsilon = 0. \quad (19)$$

2.3 Melt rate

To derive formulations for the melt rate and the heat fluxes at the ice-ocean interface, a very thin melt layer at freezing temperature is assumed. The fluxes of potential temperature and salinity across the ice-ocean interface strongly depend on the respective molecular diffusivities, $\nu^T = \nu/\text{Pr}^T$ and $\nu^S = \nu/\text{Pr}^S$, where ν is the molecular viscosity, $\text{Pr}^T = 13.8$ is the Prandtl number for temperature and $\text{Pr}^S = 2432$ is the Schmidt number for salinity.

For the derivation of the melt rate, v_b , i.e., the rate at which water is added to the ocean by means of subglacial melting, we largely follow the paper by D. M. Holland and Jenkins (1999) who compare various formulations. We adopt the well-known three-equation model that is based on flux equilibria of heat and salt across the melt layer and a linear equation for the freezing temperature. With this, the upward heat flux Q_M^T at the ice-ocean interface is composed of the diffusive heat flux Q_I^T into the ice and the latent heat flux Q_L^T needed to melt the ice:

$$Q_M^T = Q_I^T - Q_L^T, \quad (20)$$

with

$$Q_L^T = -\rho_i v_i L_i, \quad (21)$$

where L_i is the latent heat of fusion. Note that $\rho_i v_i$ is the mass of ice per unit time and unit area that is melted, such that v_i is the velocity at which the ice-ocean interface is retreating. The mass of the ocean water that is gained due to melting must be equal to the mass of ice that is melted such that $\rho_i v_i = \rho_0 v_b$, where v_b is the melt rate, i.e., the increase of sea surface height due to melting per unit time. For the flux into the ice, various formulations are available. We adopt the approach based on an advection-diffusion equation of temperature in the glacial ice, with the vertical advection velocity v_i . Based on that, the heat flux into the ice due to diffusion can be formulated as (D. M. Holland & Jenkins, 1999)

$$Q_I^T = -c_i \rho_i v_i (T_I - \theta_b), \quad (22)$$

with the heat capacity of ice, c_i , and the ice-core temperature, T_I . Note that we use here the potential freezing point temperature θ_b instead of the in-situ freezing point temperature T_b , to allow for an easy comparison with the ocean potential temperature. Combining (20) - (22), we obtain for the upward flux of temperature at the ice-ocean interface

$$f_b^T = \frac{Q_M^T}{c \rho_0} = v_b \left(\frac{c_i}{c} (\theta_b - T_I) + \frac{L_i}{c} \right), \quad (23)$$

346 with the heat capacity of sea water, c . Using the potential melt layer temperature here
 347 instead of the in-situ temperature and comparing it to the ice-core temperature here
 348 does not pose a problem, due to the large difference between melt layer and ice core tem-
 349 peratures and the typically large uncertainty in the latter.

350 Since the total salt flux into the glacial ice must be zero, the diffusive salt flux into
 351 the melt layer must be assumed to be opposite to the advective salt flux:

$$352 \quad f_b^S = \frac{Q_M^S}{\rho_0} = v_b S_b. \quad (24)$$

353 We use a linear equation for the freezing temperature, assuming that the melt layer tem-
 354 perature is at the freezing point:

$$355 \quad \theta_b = \lambda_1 S_b + \lambda_2 + \lambda_3 z_b \quad (25)$$

356 with the empirical parameters λ_1 , λ_2 and λ_3 . Note that we use slightly different empir-
 357 ical values than D. M. Holland and Jenkins (1999), to apply the potential temperature
 358 of the freezing point instead of its in-situ temperature. The new values have been cal-
 359 culated numerically by means of the function `gsw.t_freezing` of the Gibbs SeaWater
 360 (GSW) Oceanographic Toolbox of TEOS-10 at www.teos-10.org, see Tab. 1 for the mod-
 361 ified values.

362 Information about the plume properties in terms of velocity, temperature and salin-
 363 ity are required to close the melt layer computations. This will be provided by either an
 364 analytical solution for the vertical structure of the plume (Sec. 2.5) or from a numeri-
 365 cal model which uses the analytical model to consistently provide the plume informa-
 366 tion (Sec. 3.3).

367 Following Jenkins et al. (2001), the free-surface tracer boundary fluxes can be for-
 368 mulated as

$$\begin{aligned} f_{b,\text{free}}^S &= f_b^S - v_b S_b = 0, \\ f_{b,\text{free}}^T &= f_b^T - v_b \theta_b = v_b \left(\frac{c_i}{c} (\theta_b - T_I) + \frac{L_i}{c} - \theta_b \right). \end{aligned} \quad (26)$$

369 2.4 Roughness lengths for potential temperature and salinity

370 Similarly to the classical logarithmic law of the wall for velocity profiles, logarith-
 371 mic profiles are constructed for temperature and salinity in order to derive numerically
 372 consistent boundary conditions. These profiles are highly simplified and do not resolve
 373 but parameterize the effects of wall roughness and the viscous sublayer by means of sur-
 374 face roughness lengths. While the boundary condition for the velocity profiles in the melt
 375 layer (see Sec. 2.3) is a no-slip condition ($u = v = 0$), boundary values for tempera-
 376 ture and salinity in the melt layer are given by $\theta = \theta_b$ and $S = S_b$. It should however
 377 be noted that the locations for the boundary values for velocity, temperature and salin-
 378 ity are slightly different. This is due to the substantially different values for kinematic
 379 viscosity and the laminar diffusivities for θ and S . These boundary values are formally
 380 located at positions slightly above the interface $z = z_b$:

$$\begin{aligned} \theta(z = z_b - [z_0^T - z_0]) &= \theta(z' = z_0^T - z_0) = \theta_b; \\ S(z = z_b - [z_0^S - z_0]) &= S(z' = z_0^S - z_0) = S_b, \end{aligned} \quad (27)$$

382 where $z_0^T \ll z_0$ and $z_0^S \ll z_0$ are formally defined as tiny roughness lengths specific
 383 for temperature and salinity fluxes. The formulations for these roughness parameters given
 384 below have been taken from Kader and Yaglom (1972), Yaglom and Kader (1974) and
 385 Kader (1981).

386 For a hydrodynamically rough interface, the roughness length for momentum is given
 387 as

$$388 \quad z_0^{\text{rough}} = k_s \exp(-\kappa B'), \quad (28)$$

389 where k_s is the characteristic height of the roughness elements and $B' = 8.5$ is an em-
 390 pirical parameter, such that $z_0 \approx k_s/30$. For a hydrodynamically smooth interface

$$391 \quad z_0^{\text{smooth}} = \nu/u_*^b \cdot \exp(-\kappa B), \quad (29)$$

392 where $B = 5.5$ is an empirical parameter, such that $z_0 \approx 0.11 \nu/u_*^b$.

393 For both, hydrodynamically rough and smooth interfaces, the roughness scale with
 394 respect to the flux of c (where c represents any tracer such as T or S) is

$$395 \quad z_0^c = z_0 \exp\left(-\frac{\kappa}{\text{Pr}_t} \beta^c\right), \quad (30)$$

396 where the value of β^c is calculated differently for rough and smooth interfaces and $\text{Pr}_t =$
 397 ν_t/ν'_t is the turbulent Prandtl number. For a hydrodynamically rough interface,

$$398 \quad \beta_{\text{rough}}^c = 0.55 \exp\left(\frac{1}{2} \kappa B'\right) (z_0^+)^{1/2} \left((\text{Pr}^c)^{2/3} - 0.2\right) - \text{Pr}_t B' + 9.5, \quad (31)$$

399 with the non-dimensional roughness scale $z_0^+ = z_0 u_*^b / \nu$.

400 For a hydrodynamically smooth interface, (30) holds with

$$401 \quad \beta_{\text{smooth}}^c = \left(3.85 (\text{Pr}^c)^{1/3} - 1.3\right)^2 + \text{Pr}_t \left(\frac{\ln \text{Pr}^c}{\kappa} - B\right). \quad (32)$$

402 The dependence of the tracer roughness length on the Prandtl number is shown in Fig.
 403 1. Note that it is only the logarithms of the roughness lengths that are evaluated and
 404 not their direct values (which are partially too tiny to be computed). Furthermore, (30)
 405 and (32) are valid for $z_0^+ < 0.1$ and (29) and (31) are valid for $z_0^+ > 3.33$. Here we
 406 concentrate on the rough wall conditions and therefore set $z_0 = z_0^{\text{rough}}$ and $\beta^c = \beta_{\text{rough}}^c$.

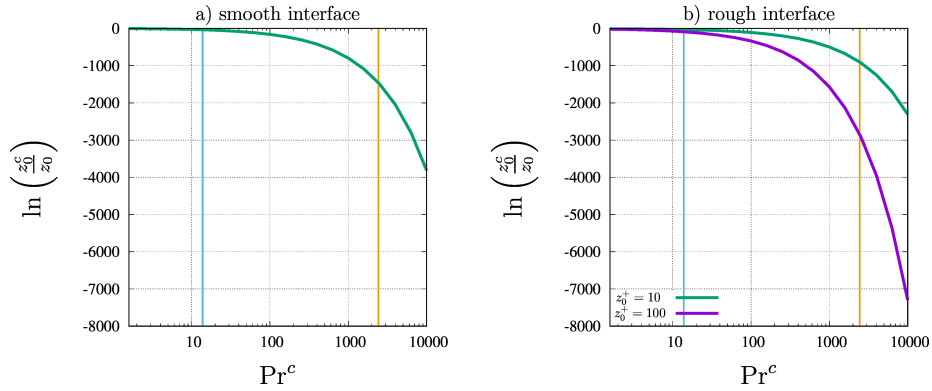


Figure 1. Logarithm of relative roughness length for tracers for a) smooth and b) rough interfaces as function of the molecular Prandtl number. The Prandtl number Pr^T for temperature (blue) and the Schmidt number Pr^S for salinity (yellow) are indicated as vertical lines. The two curves in panel b represent two different roughness lengths z_0^+ .

407

2.5 Analytical plume model

408

409

410

411

412

413

414

415

416

417

418

419

420

421

The analytical plume model that is derived here serves two purposes: It is used to construct consistent discrete formulations for the boundary conditions for θ and S (see Sec. 3) and it is used to perform an analytical parameter space study for subglacial plumes. To allow for an analytical solution, Earth rotation is neglected ($f = 0$ in equation (7)), such that only one velocity component needs to be taken into consideration. Furthermore, the interfacial slope is assumed to be positive, such that $u_*^{b,x} = u_*^b > 0$. At the plume base, turbulent entrainment of ambient water is assumed by prescribed values of friction velocity u_*^s , turbulent temperature flux f_a^T and turbulent salinity flux f_a^S . A further simplification is that for the pressure gradient force, the buoyancy of the plume is assumed to be constant: $b = \text{const}$. The profiles are formulated as a function of prescribed depth-mean values of velocity, potential temperature and salinity, \bar{u} , $\bar{\theta}$ and \bar{S} . The profiles are calculated over the entire plume thickness D , assuming parabolic eddy viscosity and eddy diffusivity. For simplicity the distance from the ice-ocean interface $z' = z_b - z$ is used as vertical reference.

422

2.5.1 Velocity profile

423

424

The derivation of the analytical stationary velocity profile under a sloping ice-ocean interface is shown in Sec. A1:

425

$$u(z') = \frac{\bar{u}}{A} \ln \left[\frac{z' + z_0}{z_0} \right] - \frac{u_*^s |u_*^s|}{\kappa u_*^b} \frac{D}{D + z_0} \left(\frac{1}{A} \ln \left[\frac{z' + z_0}{z_0} \right] + \ln \left[\frac{D - z'}{D} \right] \right), \quad (33)$$

426

427

428

429

430

431

432

where u_*^b will be calculated by means of solving the quadratic equation (A9), and A is a non-dimensional integration constant defined in (A10). The first term in (33) is the classical logarithmic law of the wall written in a form where its vertical average is \bar{u} . The second term represents the effect of the entrainment of ambient water at the plume base. It has a vertical average of zero and diverges to $\pm\infty$ for $z' \rightarrow D$, depending on the sign of u_*^s . A similar solution had been proposed by Lange and Burchard (2019) for the effect of surface wind stress in estuarine exchange flow.

433

2.5.2 Tracer profiles

434

435

436

With (A20), neglecting a tiny exponential expression in the term representing the effect of entrainment, we can formulate the analytical profiles for potential temperature ($c = \theta$) and salinity ($c = S$) as follows:

437

$$\begin{aligned} \theta(z') &= \theta_b + \frac{\text{Pr}_t f_b^T}{\kappa |u_*^b|} \left(\ln \left[\frac{z' + z_0}{z_0} \right] + \frac{\kappa}{\text{Pr}_t} \beta^T \right) \\ &\quad - \frac{\text{Pr}_t f_s^T}{\kappa |u_*^b|} \left(\frac{z_0}{D + z_0} \left(\ln \left[\frac{z' + z_0}{z_0} \right] + \frac{\kappa}{\text{Pr}_t} \beta^T \right) + \frac{D}{D + z_0} \ln \left[\frac{D - z'}{D + z_0} \right] \right), \end{aligned} \quad (34)$$

438

and

439

$$\begin{aligned} S(z') &= S_b + \frac{\text{Pr}_t f_b^S}{\kappa |u_*^b|} \left(\ln \left[\frac{z' + z_0}{z_0} \right] + \frac{\kappa}{\text{Pr}_t} \beta^S \right) \\ &\quad - \frac{\text{Pr}_t f_s^S}{\kappa |u_*^b|} \left(\frac{z_0}{D + z_0} \left(\ln \left[\frac{z' + z_0}{z_0} \right] + \frac{\kappa}{\text{Pr}_t} \beta^S \right) + \frac{D}{D + z_0} \ln \left[\frac{D - z'}{D + z_0} \right] \right), \end{aligned} \quad (35)$$

440

441

442

with the potential temperature θ_b and the salinity S_b of the melt layer. As for the velocity profile (33), also the profiles of potential temperature and salinity diverge towards $\pm\infty$ for $z' \rightarrow D$, but also here the vertical averages are finite.

443

444

445

It should be noted that the boundary values for potential temperature and salinity do not converge to θ_b and S_b for $z' \rightarrow 0$. This is also the case for the classical logarithmic laws with zero entrainment fluxes f_s^T and f_s^S . This inconsistency results from

446 the strong gradients of θ and S in the melt layer due to their small Schmidt numbers.
 447 However, since the fluxes of θ and S across the melt layer are applied as boundary con-
 448 ditions and since they are assumed to be constant within the boundary layer, this in-
 449 consistency is acceptable. This is clearly seen in the analytical profiles shown in Fig. 2b,c
 450 and the values given in the caption.

451 Vertical averaging of (34) and (35) gives

$$452 \quad \bar{\theta} - \theta_b = \frac{\text{Pr}_t f_b^T}{\kappa |u_*^b|} A_T - \frac{\text{Pr}_t f_s^T}{\kappa |u_*^b|} \left(\frac{z_0}{D + z_0} A_T - \frac{D}{D + z_0} \left(1 - \ln \left[\frac{D}{D + z_0} \right] \right) \right), \quad (36)$$

453 and

$$454 \quad \bar{S} - S_b = \frac{\text{Pr}_t f_b^S}{\kappa |u_*^b|} A_S - \frac{\text{Pr}_t f_s^S}{\kappa |u_*^b|} \left(\frac{z_0}{D + z_0} A_S - \frac{D}{D + z_0} \left(1 - \ln \left[\frac{D}{D + z_0} \right] \right) \right), \quad (37)$$

455 with the integration constants A_T and A_S calculated according to (A22). By combin-
 456 ing (34) and (35) with (36) and (37), a formulation of the profiles is obtained that de-
 457 pends on prescribed values of the depth-averaged potential temperature $\bar{\theta}$ and salinity
 458 \bar{S} . The melt layer freezing temperature and melt layer salinity θ_b and S_b can now be de-
 459 termined, using the melt layer formulation given in Sec. 2.3. Combining equations (23)
 460 and (24) for the interface fluxes of potential temperature and salinity, the linear freez-
 461 ing temperature formulation (25) with the vertically averaged equations (36) and (37)
 462 for potential temperature and salinity of the plume gives five equations for the five un-
 463 knowns f_b^T , f_b^S , v_b , T_b and S_b . These equations are combined in a way that a quadratic
 464 equation for S_b results, of which the positive solution is the physically correct one.

465 **2.5.3 Analytical examples**

466 Two sets of plume profiles are calculated, without entrainment at the plume base
 467 (experiment N) and with entrainment at the plume base (experiment E). Results for u ,
 468 θ and S are shown in Fig. 2, using the empirical parameters given in table 1. For both
 469 experiments, bulk values of the plume thickness $D = 20$ m, the depth-mean velocity
 470 $\bar{u} = 0.2 \text{ m s}^{-1}$, the depth-mean temperature $\bar{\theta} = -1.75^\circ\text{C}$, the depth-mean salinity $\bar{S} =$
 471 33.1 g kg^{-1} , the interfacial depth $z_b = -300$ m, and an interfacial roughness length of
 472 $z_0 = 10^{-2}$ m are prescribed. These values are similar to those at the end of the tran-
 473 sient default experiment from Sec. 4.2.1. Results are shown in linear and logarithmic scale.

474 For the experiment without entrainment, the profiles of velocity, temperature and
 475 salinity are exactly logarithmic (Fig. 2d-f). Due to the small Schmidt numbers, the slopes
 476 of the temperature and salinity profiles are very small. In the case of salinity, the dif-
 477 ference across the full depth of the plume is about only $6 \cdot 10^{-3} \text{ g kg}^{-1}$, such that in the
 478 non-logarithmic presentation (Fig. 2c), vertical salinity gradients can not be detected by
 479 visual inspection. A striking feature of the analytical temperature and salinity profiles
 480 is the substantial difference between the melt layer values, θ_b and S_b , and the bound-
 481 ary values, $\theta(z_b)$ and $S(z_b)$, see Fig. 2b,c. This is a direct consequence of (27), and does
 482 not pose a practical problem, because it is not the boundary values that are applied, but
 483 the fluxes of temperature and salinity which are assumed to be constant on the scale of
 484 the melt layer thickness. There is a conceptual issue, because the construction of the free-
 485 surface boundary conditions assumes that melt layer values and boundary values are iden-
 486 tical (see Jenkins et al., 2001, and Eq. (26) of this study). Since these free-surface bound-
 487 ary conditions are not used here, it is beyond the scope of the present study to resolve
 488 this inconsistency.

489 The analytical solution including fluxes of momentum, temperature and salinity
 490 across the base of the plume (exp. E, Fig. 2g-l) allows to mimic entrainment of ambi-
 491 ent water. The entrainment fluxes are estimated as follows:

$$492 \quad u_*^s |u_*^s| = -v_e (\bar{u} - u_0), \quad f_s^T = -v_e (\bar{\theta} - \theta_0), \quad f_s^S = -v_e (\bar{S} - S_0), \quad (38)$$

492 with the entrainment velocity $v_e = 0.036 \bar{u} \sin \alpha$, see Jenkins (1991) and Sec. 4.3, and
 493 the ambient values are chosen to be the same as in the default scenario of the transient
 494 simulations presented in Sec. 4.2.1: $\tan \alpha = 0.005$, $u_0 = 0$, $\theta_0 = 1^\circ\text{C}$ and $S_0 = 34.5$
 495 g kg^{-1} . With the above parameters, we obtain $v_e = 3.6 \cdot 10^{-5} \text{ m s}^{-1}$, $u_*^s = -7.6 \cdot 10^{-6} \text{ m s}^{-1}$,
 496 $f_s^T = 9.9 \cdot 10^{-5} \text{ K m s}^{-1}$ and $f_s^S = 5.0 \cdot 10^{-5} \text{ g kg}^{-1} \text{ m s}^{-1}$.

497 As a result, the entrainment has only a minimal influence on the velocity and salin-
 498 ity profiles (Figs. 2g,j and 2i,l). However, the temperature profile (Figs. 2h,k) shows slightly
 499 larger vertical gradients due to the entrainment of relatively warm water. Due to the sta-
 500 tionary character of the analytical solution with fixed values of \bar{u} , $\bar{\theta}$ and \bar{S} , there is no
 501 predictive skill. The melt rate ($v_m = 5.22 \text{ m y}^{-1}$) and the ocean-to-ice heat flux ($Q_M^T =$
 502 63 W m^{-2}) depend only weakly on the entrainment. But due to entrainment of warm
 503 and salty ambient water, the instantaneous trends in average plume temperature and
 504 salinity are changed from $\partial_t \bar{T} = -6.3 \cdot 10^{-2} \text{ K day}^{-1}$ to $\partial_t \bar{T} = +0.37 \text{ K day}^{-1}$ and
 505 from $\partial_t \bar{S} = -2.2 \cdot 10^{-2} \text{ g kg}^{-1} \text{ day}^{-1}$ to $\partial_t \bar{S} = +0.19 \text{ g kg}^{-1} \text{ day}^{-1}$.

Variable	Meaning	Value	Unit
c	heat capacity of sea water	4180.0	$\text{J kg}^{-1} \text{K}^{-1}$
c_i	heat capacity of glacial ice	1995.0	$\text{J kg}^{-1} \text{K}^{-1}$
κ	van Karman number	0.4	–
λ_1	parameter in freezing temperature equation	-0.0567	$\text{K (g kg}^{-1})^{-1}$
λ_2	parameter in freezing temperature equation	0.0754	K
λ_3	parameter in freezing temperature equation	$7.68 \cdot 10^{-4}$	K m^{-1}
L_i	latent heat of fusion	$3.335 \cdot 10^5$	J kg^{-1}
Pr_t	turbulent Prandtl number	0.7	–
Pr^T	molecular Prandtl number for T	13.8	–
Pr^S	molecular Prandtl number for S	2432.0	–
ν	molecular viscosity	$1.95 \cdot 10^{-6}$	$\text{m}^2 \text{s}^{-1}$
ρ_0	reference density of ocean water	1027	kg m^{-3}
ρ_i	density of glacial ice	910	kg m^{-3}
T_I	ice core temperature	-20.0	$^\circ\text{C}$

Table 1. Table summarising the empirical parameters used in the present study.

506 3 Numerical implementation

507 In numerical models, the analytical logarithmic profiles for u , θ and S derived in
 508 Sec. 2.5 can be used to calculate fluxes of momentum, temperature and salinity at the
 509 ice-ocean interface in a consistent and convergent way. To do so, we assume that within
 510 the first grid layer underneath the ice-ocean interface the logarithmic laws (33), (34) and
 511 (35) are valid, neglecting the fluxes across the plume base ($u_*^s = f_s^T = f_s^S = 0$), such
 512 that the formulations reduce to

$$513 \quad u(z') = \frac{u_*^{b,x}}{\kappa} \ln \left[\frac{z' + z_0}{z_0} \right], \quad v(z') = \frac{u_*^{b,y}}{\kappa} \ln \left[\frac{z' + z_0}{z_0} \right], \quad (39)$$

$$514 \quad \theta(z') = \theta_b + \frac{\text{Pr}_t f_b^T}{\kappa u_*^b} \left(\ln \left[\frac{z' + z_0}{z_0} \right] + \frac{\kappa}{\text{Pr}_t} \beta^T \right), \quad (40)$$

516 and

$$517 \quad S(z') = S_b + \frac{\text{Pr}_t f_b^S}{\kappa u_*^b} \left(\ln \left[\frac{z' + z_0}{z_0} \right] + \frac{\kappa}{\text{Pr}_t} \beta^S \right), \quad (41)$$

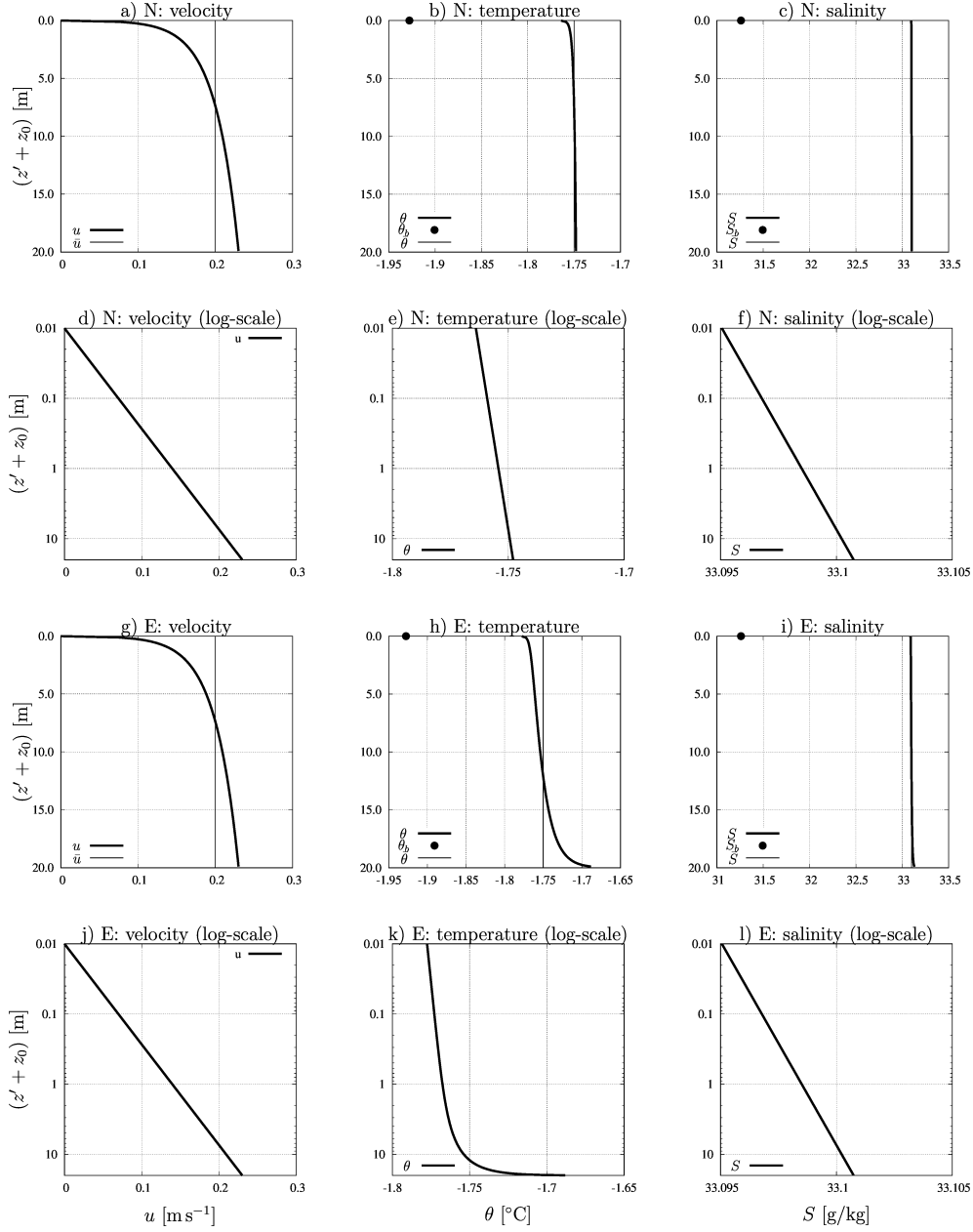


Figure 2. Analytical solutions for velocity (panels a, d, g j), potential temperature (panels b, e, h, k) and salinity (panels c, f, i, l) for experiments N (without entrainment, panels a-f) and E (with entrainment panels g-l). Parameter values are given in Tab. 1. Profiles are shown as bold lines in linear (panels a-c,g-i) and logarithmic (panels d-f, j-l) depth scale. Prescribed depth mean values \bar{u} , $\bar{\theta}$ and \bar{S} are shown as thin lines. Boundary values $T(z_b - (z_0 - z_0^T)) = T_b$, and $S(z_b - (z_0 - z_0^S)) = S_b$, are shown as symbols. Note that $S_b = 31.26 \text{ g kg}^{-1}$ is substantially smaller than $S(z_b) = 33.09 \text{ g kg}^{-1}$, and $\theta_b = -1.93 \text{ }^\circ\text{C}$ is substantially smaller than $\theta(z_b) = -1.76 \text{ }^\circ\text{C}$.

518 where we have extended the analytical solution to the full velocity vector (u, v) . Note,
 519 that the analytical profiles (39) - (41) are expected to hold in some vicinity of the in-
 520 terface only, depending on the forcing of the plume.

521 3.1 Momentum fluxes

522 Let in a numerical model $u(z'_{k_{\max}}) = u_{k_{\max}}$ and $v(z'_{k_{\max}}) = v_{k_{\max}}$ denote the upper-
 523 layer velocity vector with the upper layer thickness $h_{k_{\max}}$ and $z'_{k_{\max}} = \frac{1}{2}h_{k_{\max}}$. Then
 524 (39) gives

$$525 \quad u_{k_{\max}} = \frac{u_*^{b,x}}{\kappa} \ln \left(\frac{\frac{1}{2}h_{k_{\max}} + z_0}{z_0} \right), \quad v_{k_{\max}} = \frac{u_*^{b,y}}{\kappa} \ln \left(\frac{\frac{1}{2}h_{k_{\max}} + z_0}{z_0} \right), \quad (42)$$

526 such that

$$527 \quad u_*^{b,x} u_*^b = c_d u_{k_{\max}} (u_{k_{\max}}^2 + v_{k_{\max}}^2)^{1/2}, \quad u_*^{b,y} u_*^b = c_d v_{k_{\max}} (u_{k_{\max}}^2 + v_{k_{\max}}^2)^{1/2}, \quad (43)$$

528 with the numerical drag coefficient

$$529 \quad c_d = \left(\frac{\kappa}{\ln \left(\frac{\frac{1}{2}h_{k_{\max}} + z_0}{z_0} \right)} \right)^2. \quad (44)$$

530 This is the numerically consistent discretization for the momentum flux at the ice-ocean
 531 interface as defined in (15). At the same time, (43) with (44) also satisfy the no-slip con-
 532 dition (14) for u and v , since with fixed left-hand sides in (43) a decreasing surface layer
 533 thickness $h_{k_{\max}}$ will lead to unbounded growth of c_d and thus convergence of $u_{k_{\max}}$ and
 534 $v_{k_{\max}}$ towards zero. This numerical treatment of a frictional boundary layer is applied
 535 in many ocean models for the bottom boundary layer (Klingbeil et al., 2018, their Sec. 7.6).
 536 If, however, a constant value for c_d is chosen that does not depend on resolution, then
 537 a refined resolution near the boundary will not result in a reduction of velocity and con-
 538 sequently in an underestimation of shear and friction velocity (see Sec. 3.4).

539 3.2 Tracer fluxes

540 The calculations of the temperature and salinity fluxes are carried out in a simi-
 541 lar way than the momentum fluxes. When for the discrete profiles of temperature and
 542 salinity, $\theta(z'_{k_{\max}}) = \theta_{k_{\max}}$ and $S(z'_{k_{\max}}) = S_{k_{\max}}$ with $z'_{k_{\max}} = \frac{1}{2}h_{k_{\max}}$ and the upper
 543 layer thickness $h_{k_{\max}}$ are known, the following relations can be derived from the loga-
 544 rithmic tracer laws (40) and (41):

$$545 \quad \theta_{k_{\max}} = \theta_b + \frac{\text{Pr}_t f_b^T}{\kappa u_*^b} \left(\ln \left[\frac{\frac{1}{2}h_{k_{\max}} + z_0}{z_0} \right] + \frac{\kappa}{\text{Pr}_t} \beta^T \right), \quad (45)$$

546 and

$$547 \quad S_{k_{\max}} = S_b + \frac{\text{Pr}_t f_b^S}{\kappa u_*^b} \left(\ln \left[\frac{\frac{1}{2}h_{k_{\max}} + z_0}{z_0} \right] + \frac{\kappa}{\text{Pr}_t} \beta^S \right). \quad (46)$$

548 Note that (45) and (46) can be reformulated as

$$549 \quad f_b^T = \gamma^T (\theta_{k_{\max}} - \theta_b) \quad (47)$$

550 and

$$551 \quad f_b^S = \gamma^S (S_{k_{\max}} - S_b) \quad (48)$$

552 with the exchange velocities

$$553 \quad \gamma^T = \frac{\kappa u_*^b}{\text{Pr}_t \ln \left(\frac{\frac{1}{2}h_{k_{\max}} + z_0}{z_0} \right) + \kappa \beta^T} \quad (49)$$

554 and

$$555 \quad \gamma^S = \frac{\kappa u_*^b}{\text{Pr}_t \ln \left(\frac{\frac{1}{2} h_{k_{\max}} + z_0}{z_0} \right) + \kappa \beta^S} \quad (50)$$

556 with the coefficients β^T and β^S from (31) or (32). With (23), (24), (25), (47) and (48)
 557 we have now five equations to solve for the five unknowns T_b , S_b , v_b , f_b^T and f_b^S . Note
 558 that we solve this system of equations in order to calculate the melt rate v_b which is ap-
 559 plied to add fresh and cold water to the ocean surface due to subglacial melting, see Sec. 3.3
 560 for the implementation.

561 3.3 Free-surface versus rigid-lid models

562 For a free-surface model, $h_{k_{\max}}^n$ and the tracer concentration $X_{k_{\max}}^n$ should be dis-
 563 cretized as follows (assuming zero volume and tracer fluxes across the interface at the
 564 bottom of the layer):

$$565 \quad \frac{h_{k_{\max}}^{n+1} - h_{k_{\max}}^n}{\Delta t} = v_b^n, \quad (51)$$

566 and

$$567 \quad \frac{X_{k_{\max}}^{n+1} h_{k_{\max}}^{n+1} - X_{k_{\max}}^n h_{k_{\max}}^n}{\Delta t} = - (f_{b,\text{free}}^X)^n, \quad (52)$$

568 which can be combined into

$$569 \quad h_{k_{\max}}^{n+1} \frac{X_{k_{\max}}^{n+1} - X_{k_{\max}}^n}{\Delta t} = -v_b^n X_{k_{\max}}^n - (f_{b,\text{free}}^X)^n, \quad (53)$$

570 where the superscript indicates the number of the time step. For a rigid-lid model as ap-
 571 plied in the present study, the numerical scheme (53) will apply, but with a constant layer
 572 thickness $h_{k_{\max}}$:

$$573 \quad \frac{X_{k_{\max}}^{n+1} - X_{k_{\max}}^n}{\Delta t} = - \frac{v_b^n X_{k_{\max}}^n + (f_{b,\text{free}}^X)^n}{h_{k_{\max}}}, \quad (54)$$

574 where the respective free-surface fluxes for temperature and salinity are calculated ac-
 575 cording to (26).

576 3.4 Numerical convergence experiment

577 To test the numerical methods developed in Sec. 3.1 - 3.3, the momentum equa-
 578 tion (7) for non-rotational flow ($f = 0$ and $v = 0$) and the temperature and salinity
 579 equations (9) were discretized. The entire water column was accelerated by a barotropic
 580 (constant in space) pressure gradient in a way that the prescribed depth-averaged plume
 581 velocity of \bar{u} resulted. Additionally to the melt fluxes, temperature and salinity were forced
 582 with a depth-independent source/sink term compensating for the freshening and cool-
 583 ing, see (A18). Empirical parameters were chosen identically to Experiment N in Sec. 2.5.3,
 584 such that an analytical solution is available for quantifying the accuracy of the numer-
 585 ical scheme for different vertical resolutions and treatments of the melt flux parameter-
 586 ization.

587 An Euler-forward central-difference discretization of these diffusion equations was
 588 applied with a sufficiently small time step. The numerical scheme was executed until a
 589 stationary numerical solution was approximated at high accuracy. Three different ver-
 590 tical discretizations were chosen, ranging from very coarse to very fine (see details in the
 591 caption of Tab. 2).

592 For each vertical resolution, three different numerical treatments of the melt fluxes
 593 were chosen:

- 594 1. The high-resolution accurate treatment as given by (42), (45) and (46) with the
 595 analytical logarithmic laws for momentum and tracers.

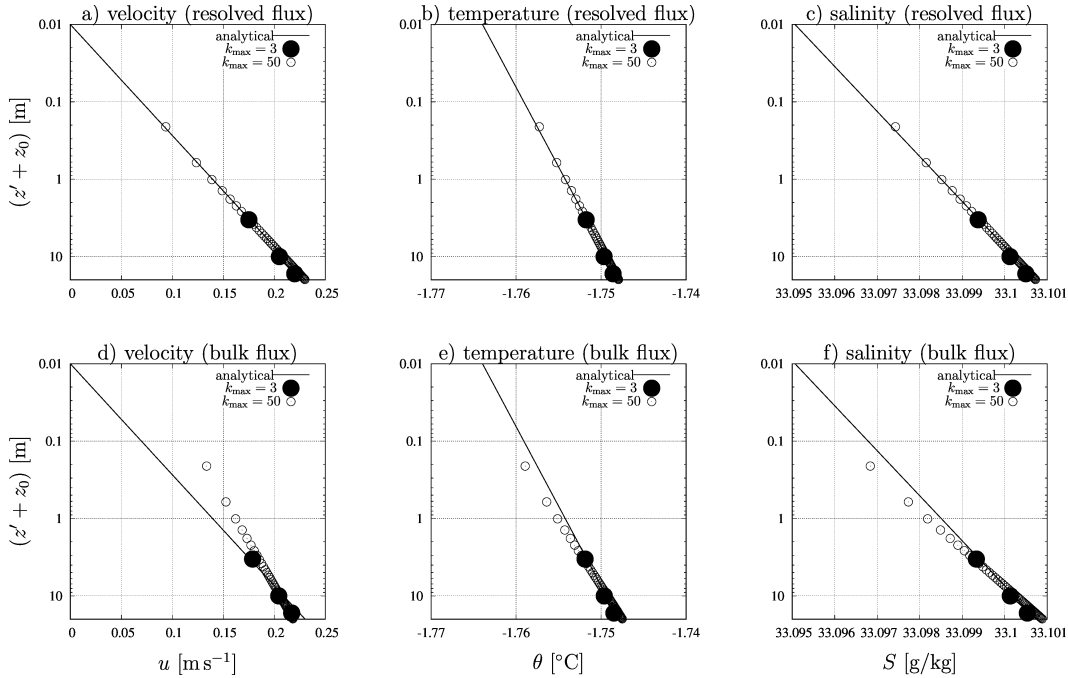


Figure 3. Numerical simulation of experiment N without entrainment at the plume base: Numerical simulations for velocity u (panels a & d) potential temperature θ (panels b & e) and salinity S (panels c & f) in logarithmic scale using values given in table 1. The analytical solution is shown by a black line, the numerical solutions are shown by large black dots ($k_{\max} = 3$) and small circles ($k_{\max} = 50$). Panels a-c show profiles obtained from the high-resolution numerical flux calculations derived in Sec. 3.1 and 3.2 (method 1). In panels d-f numerical profiles are shown where bulk flux parameterizations were used by inserting in the formulations (42) - (50) the plume thickness D instead of the upper layer thickness $h_{k_{\max}}$ and the plume-average values \bar{u} , $\bar{\theta}$ and \bar{S} instead of the upper layer values $u_{k_{\max}}$, $\theta_{k_{\max}}$ and $S_{k_{\max}}$ (method 3).

- 592 2. The high-resolution formulation (42) for momentum, but bulk values across the
 593 entire plume thickness for the tracer fluxes, i.e., using (45) and (46) with the plume
 594 thickness D instead of the upper layer thickness $h_{k_{\max}}$ and the plume-average val-
 595 ues $\bar{\theta}$ and \bar{S} instead of the upper layer values $\theta_{k_{\max}}$ and $S_{k_{\max}}$.
 596 3. Similar to 2., but now also for the momentum flux calculation a bulk formulation
 597 is used by using (42) with D and \bar{u} instead of $h_{k_{\max}}$ and $u_{k_{\max}}$.

598 Numerical results for method 1 are shown in Fig. 3a-c against the analytical solution for
 599 two different resolutions. The results are highly accurate, even for the coarse resolution
 600 with only three layers inside the plume. Results for method 2 are very similar (not shown).
 601 This means that the bulk formulation for the tracer fluxes is still valid because of the
 602 high vertical homogeneity of the tracer profiles with $\theta_{k_{\max}} \approx \bar{\theta}$ and $S_{k_{\max}} \approx \bar{S}$ and γ^T
 603 and γ^S being largely independent of the layer thickness. In contrast, method 3 diverges
 604 from the analytical reference solution (see Fig. 3d-f), since the bulk formulation for the
 605 momentum flux is decreasingly representative for increasing resolution with c_d not in-
 606 creasing towards ∞ .

607 Since the accurate calculation of the melt rate v_b is one of the main goals of refined
 608 numerical simulations, it is given in Tab. 2 for all numerical experiments (three resolu-
 609 tions and three melt flux formulations). For the consistent melt flux formulation 1, melt

		u resolved θ & S resolved Fig. 3a-c	u resolved θ & S bulk	u bulk θ & S bulk Fig. 3d-f
analytical		5.2236		
$k_{\max} = 3$;	$h_{k_{\max}} = 6.66$ m	5.2070	5.1962	4.7888
$k_{\max} = 50$;	$h_{k_{\max}} = 0.4$ m	5.2710	5.2546	4.0944
$k_{\max} = 200$;	$h_{k_{\max}} = 0.015$ m	5.2360	5.2226	3.6353

Table 2. Numerical simulation of experiment N without entrainment at the plume base: Calculated subglacial melt rates in m y^{-1} for various vertical resolutions and different treatments of fluxes, compared to the analytical melt rate. The very high resolution for $k_{\max} = 200$ layers was obtained by logarithmic zooming towards the ice-ocean interface.

610 rates converge towards the analytical value of 5.2236 m y^{-1} . In the range of the reso-
611 lutions tested here, method 2 shows an almost indistinguishable behaviour, although it
612 should formally not converge towards the analytical solution. Also for the coarse reso-
613 lutions both methods 1 and 2 give relatively accurate values with only about 3-4 % error
614 for the very coarse resolution. In contrast to this, the bulk method 3 for calculat-
615 ing momentum fluxes diverges substantially, and gives an error of about 1.1 m y^{-1} (22
616 %) for a top-layer resolution of $h_{k_{\max}} = 0.4$ m, and an error of 1.6 m y^{-1} (30 %)
617 for the very high resolution of $h_{k_{\max}} = 0.015$ m. Therefore, it is highly recommended to use
618 methods 1 or 2 for the momentum and tracer fluxes, with a preference for the fully con-
619 sistent method 1.

620 4 Transient numerical experiments

621 The General Ocean Turbulence Model (GOTM, Burchard and Bolding (2001); Um-
622 lauf and Burchard (2005); Li et al. (2021), see also www.gotm.net), a one-dimensional
623 water-column model coupled to a library of turbulence closure models, was modified to
624 reproduce the vertical structure of subglacial plumes. For the surface, i.e., the ice-ocean
625 interface, no-slip conditions for velocity (14) and fluxes of salinity and heat due to melt
626 processes at the ice-ocean interface (16) were added. Since GOTM treats surface fresh-
627 water fluxes like a rigid-lid model (i.e., considering changes in concentrations instead of
628 changes in volume), the fluxes of salinity and heat have been implemented according to
629 (54). A further change to GOTM needed to reproduce subglacial plumes was the applica-
630 tion of pressure gradients due to vertical buoyancy gradients under a sloping ice-ocean
631 interface, as described in (5). As turbulence closure model, the k - ε model with the quasi-
632 equilibrium second-moment closure by Y. Cheng et al. (2002) was used.

633 4.1 Model setup

634 The simulations analysed here start from rest (zero velocity). The initial values of
635 potential temperature and salinity within the plume of initially $D = 5$ m thickness rep-
636 resent ambient seawater mixed with fresh water at freezing temperature to mimic sub-
637 glacial discharge at the grounding line (supposed to be at a depth of $z_b = -300$ m).
638 The depth of the water column is chosen to be 150 m, such that the bottom at $z = -450$
639 m is sufficiently deep to allow for an undisturbed plume deepening for all sensitivity stud-
640 ies. The vertical discretisation uses $k_{\max} = 500$ layers with zooming towards the ice-
641 ocean interface such that the resolution is gradually increasing from $h_1 = 0.5$ m at the

642 bottom to $h_{k_{\max}} = 0.09$ m at the surface. In a sensitivity study about the effects of coarser
 643 vertical resolution, a total of only 50 or 25 layers will be used (Sec. 4.2.3).

644 The ambient water is at rest and has a high ocean salinity of $S_0 = 34.5 \text{ g kg}^{-1}$ and
 645 potential temperatures of $\theta_0 = 1^\circ\text{C} \pm 1^\circ\text{C}$ (depending on the scenario). The initial plume
 646 salinity and potential temperature are $S = 32 \text{ g kg}^{-1}$ and $\theta = -1^\circ\text{C}$, such that its po-
 647 tential density ρ is lower than the potential density ρ_0 of the plume water. With this,
 648 the initial pressure gradient drives a subglacial plume rising upwards along the slope of
 649 the ice-ocean interface. The latitude of the water column location is 79°N , such that the
 650 Coriolis parameter has a value of $f = 1.43 \cdot 10^{-4} \text{ s}^{-1}$. The ice-ocean interface is slop-
 651 ing towards the north, while the slope toward the east vanishes ($\alpha_x = 0$). During the
 652 simulation time of 14 days, the plume velocity is expected to point towards the north-
 653 east ($u, v > 0$) directions as a consequence of the force balance between northward pres-
 654 sure gradient force, Coriolis force and frictional effects. The plume is subject to cooling
 655 and freshening due to melt fluxes at the ice-ocean interface and to warming and salin-
 656 ification due to entrainment of warmer and saltier ambient water. This simulation can
 657 be thought of as a plume underneath an infinite plain, where all plume properties are
 658 homogeneous along the interfacial slope (Arneborg et al., 2007), and all thermodynamic
 659 effects of the interfacial slope are ignored.

660 We analyse one default simulation in detail and carry out six sensitivity simula-
 661 tions with variations in northward slope α_y , interfacial roughness z_0 and ambient tem-
 662 perature θ_0 . The parameters for the sensitivity study are given in table 3.

	high	default	low
	ayp	def	aym
$\tan \alpha_y$:	$2.5 \cdot 10^{-2}$	$5 \cdot 10^{-3}$	$1 \cdot 10^{-3}$
	z0p	def	z0m
z_0^b :	$1 \cdot 10^{-1} \text{ m}$	$1 \cdot 10^{-2} \text{ m}$	$1 \cdot 10^{-3} \text{ m}$
	tap	def	tam
θ_0 :	2°C	1°C	0°C

Table 3. Parameter settings for the default simulation (**def**) and sensitivity simulations with high (**ayp**) and low (**aym**) values for the interfacial slope α_y , high (**z0p**) and low (**z0m**) values for the interfacial roughness z_0^b and high (**tap**) and low (**tam**) values for the ambient temperature θ_0 .

663 **4.1.1 Analysis of bulk values**

664 According to Arneborg et al. (2007), the bulk properties of the plume can be di-
 665 agnosed from individual profiles as follows:

$$\begin{aligned}
 \bar{b}D &= \int_{-\infty}^{z_b} b \, dz, \\
 \bar{b}D^2 &= 2 \int_{-\infty}^{z_b} b(z_b - z) \, dz, \\
 (\bar{u}D, \bar{v}D) &= \int_{-\infty}^{z_b} (u, v) \, dz,
 \end{aligned}
 \tag{55}$$

667 with the plume thickness D , the depth-averaged buoyancy \bar{b} , and the depth-averaged plume
 668 velocity vector (\bar{u}, \bar{v}) . The vertically averaged plume speed is defined as $\bar{u}_s = (\bar{u}^2 + \bar{v}^2)^{1/2}$.

Depth-averaged salinity and potential temperature are defined accordingly:

$$\bar{S} = \frac{1}{D} \int_{-\infty}^{z_b} (S - S_0) dz + S_0 \text{ and } \bar{\theta} = \frac{1}{D} \int_{-\infty}^{z_b} (\theta - \theta_0) dz + \theta_0. \quad (56)$$

Characteristic non-dimensional parameters of the plume dynamics are the Froude number (ratio of flow velocity to phase velocity of long interfacial waves)

$$\text{Fr} = \frac{\bar{u}_s}{\sqrt{\bar{b}D \cos \alpha}}, \quad (57)$$

where $\text{Fr} > 1$ marks supercritical flow and $\text{Fr} < 1$ marks subcritical flow, the Ekman number (ratio of frictional to rotational effects)

$$K = \frac{c_d \bar{u}_s}{fD} \quad (58)$$

and the bulk Richardson number (ratio of bulk stratification to bulk shear)

$$\text{Ri}_b = \frac{\bar{b}D}{\bar{u}_s^2} \approx \text{Fr}^{-2}, \quad (59)$$

which we need to define for the entrainment formulation by Jungclaus and Backhaus (1994). For the Froude number, the overall slope angle is calculated as

$$\alpha = \arctan \left(\tan^2 \alpha_x + \tan^2 \alpha_y \right)^{1/2}. \quad (60)$$

4.2 Model Results

4.2.1 Default scenario

In the default scenario, the plume thickness increases from its initial value of $D = 5$ m to about $D = 20$ m within 14 days (Fig. 4). In the initial phase, the plume is accelerated northwards along the slope due to the pressure gradient force, reaching up to a depth-averaged value of $\bar{v} = 0.25 \text{ m s}^{-1}$ within one hour (Fig. 5a). In this initial phase, the flow is supercritical ($\text{Fr} > 1$) for a short time (Fig. 5b). Afterwards, due to Earth rotation, the plume velocity veers towards the cross-slope direction (Fig. 4a,b). This effect is strongest at the plume base where frictional and rotational effects combine in a complex way (Fig. 6d), see Fig. 11 of Umlauf et al. (2010) for details. During the further development of the plume, frictional effects are reduced due to increased plume thickness and decreased velocity (expressed as strongly decreasing Ekman number, see Fig. 5b), such that the depth-averaged velocity vector (\bar{u}, \bar{v}) is further veering towards the downslope direction (Fig. 5a), with the downslope velocity peak remaining at the plume base. After the initial adjustment phase, the plume is close to a dynamic balance as indicated by the relatively close agreement between plume velocity diagnosed from the simulation result and the analytical equilibrium velocity diagnosed from the dynamic steady-state assumption of the vertically integrated momentum equations (see Appendix B).

After the initialization, the flow becomes subcritical, with the Froude number slowly decreasing to $\text{Fr} = 0.6$ at the end of the simulation (Fig. 5b). The square root of the vertically integrated and thus the shallow-water speed $(\bar{b}D)^{1/2}$ is slowly increasing during simulation due to the buoyancy fluxes at the ice-ocean interface (Fig. 5a). For no such buoyancy fluxes theory predicts a constant shallow water speed (Arneborg et al., 2007). Potential temperature and salinity are quickly approaching relatively constant values, suggesting a balance between melt fluxes and entrainment fluxes (Fig. 4c,d).

Since the vertical structure of the plume is almost self-similar after the initial adjustment (Arneborg et al., 2007), the vertical profiles of plumes properties shown in Fig. 6 at the end of the simulation time are largely representative for the plume in dynamical balance. When rotating the velocity vector profiles into the direction of the depth

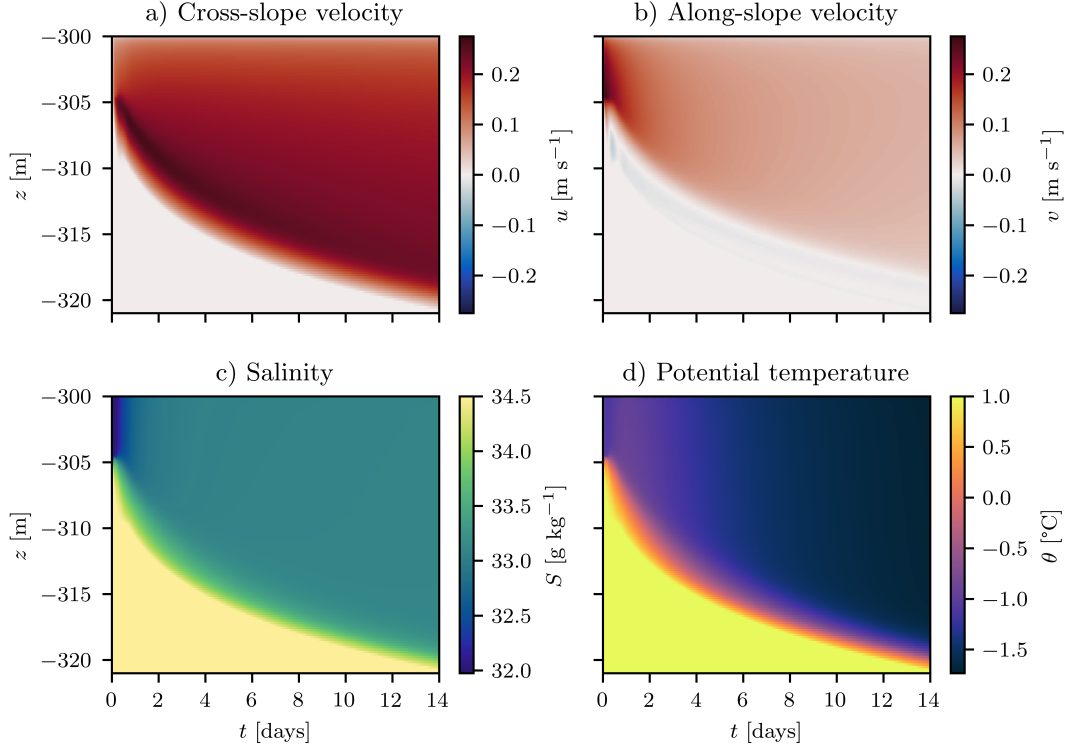


Figure 4. Simulated cross-slope and along-slope velocity, salinity and potential temperature profiles for the default scenario `def` during the 14-day simulation period.

711 mean flow vector, it becomes evident that the velocity peak at the plume base is most
 712 pronounced in the cross-flow velocity component (Fig. 6a). In the frictionally dominated
 713 part of the plume, the cross-flow velocity is negative due to Ekman dynamics (Umlauf
 714 & Arneborg, 2009; Umlauf et al., 2010). Potential temperature and salinity are well-mixed
 715 in the bulk of the plume, with a gradual increase in stratification at the plume base (Fig.
 716 6b,c). The entire plume is stably stratified (Fig. 6d). Most of the stratification seems
 717 to be due to entrainment of denser water from below, but the increase of N^2 towards
 718 the ice-ocean interface indicates that some stratification is also induced by the stabil-
 719 ising ocean-to-ice fluxes. Due to the strong shear at the ice-ocean interface (Fig. 6e), the
 720 gradient Richardson number decreases continuously in upward direction. It has a max-
 721 imum of about $Ri = 0.75$ directly above the entrainment layer. It is characteristic of
 722 two-equation turbulence closure models that they allow active mixing at such high sta-
 723 bility conditions due to vertical turbulent transport of TKE (Umlauf, 2009). In the en-
 724 trainment layer itself, Ri attains the value of the steady-state gradient Richardson num-
 725 ber of $Ri_{st} = 0.25$, which is a result of the calibration procedure of the two-equation
 726 turbulence closure model (Burchard & Baumert, 1995; Umlauf & Burchard, 2005). The
 727 rotated stress vector ($\hat{\tau}^x, \hat{\tau}^y$) and the eddy viscosity ν_t are compared to the analytical
 728 formulations from (A3) and (A4) in Fig. 6g,h, using the simulated surface stress and a
 729 mixed-layer depth diagnosed from the first zero-crossing of the simulated shear stress.
 730 For the shear stress the agreement is very good, but the parabolic analytical eddy vis-
 731 cosity overestimates the simulated profile by about one third, because it does not take
 732 into account effects of stratification that are present at the base of the plume. Still near
 733 the ice-ocean interface, the agreement between simulated and analytical eddy viscosity
 734 is very good, and both profiles converge to $\kappa(z' + z_0)$ near the interface. For the sim-
 735 ulated profile, this is a consequence of the formulation of the Schmidt number in the ε -

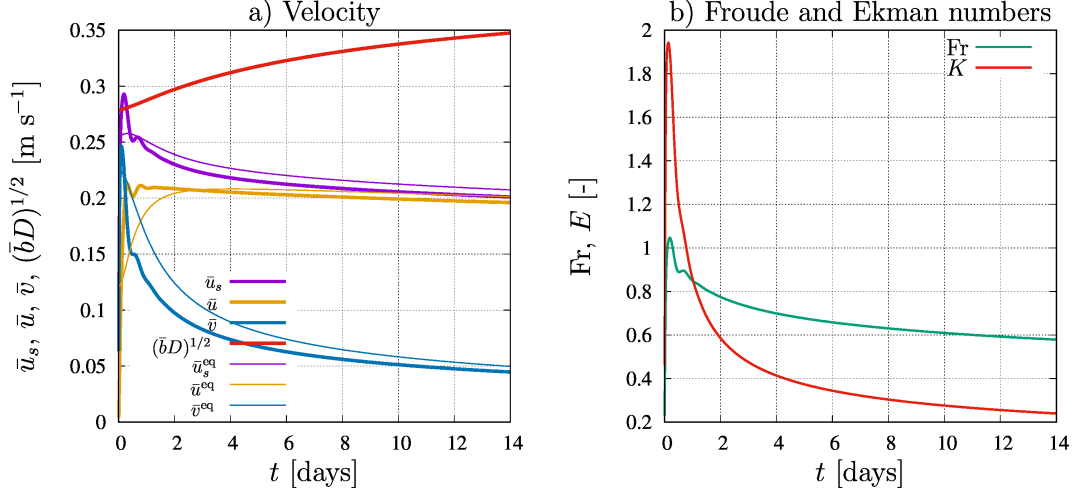


Figure 5. Time series of a) depth-averaged velocity diagnosed from GOTM and equilibrium velocity predicted by the steady-state theory presented in Appendix B as well as the phase velocity and b) Froude and Ekman numbers for the `def` scenario.

736 equation of the turbulence closure model (Burchard & Baumert, 1995; Umlauf & Bur-
 737 chard, 2005) for which the resulting ε -profile is shown in Fig. 6i.

738 4.2.2 Sensitivity to forcing parameters

739 In the default scenario described in Sec. 4.2.1, the entrainment velocity v_e is about
 740 1 to 2 orders of magnitude larger than the melt velocity v_m , with peak values of v_e reach-
 741 ing almost 2 km y⁻¹, while the melt velocity has maximum values of about 20 m y⁻¹ (ma-
 742 genta lines in Fig. 7). With that, the assumption of a rigid lid does not significantly in-
 743 fluence the plume thickness. Highest entrainment and melt velocities are reached in the
 744 early adjustment phase of the plume due to maximum Froude and Ekman numbers (Fig.
 745 5) after which a steady decrease is observed.

746 Increasing or decreasing the slope of the ice-ocean interface by a factor of 5 in the
 747 scenarios `ayp` and `aym`, has significant effects on the development of the plume. The steeper
 748 slope more than triples the final plume thickness to more than $D = 75$ m, with entrain-
 749 ment velocities of up to $v_e = 20$ km y⁻¹ and melt velocities of up to almost $v_m = 70$
 750 m y⁻¹ (Fig. 7a,d,g). In contrast, the scenario `aym` with the strongly decreased slope (Tab.
 751 3), leads to on a very weak increase in plume thickness during the 14-day simulation, with
 752 entrainment velocities of about $v_e = 20$ m y⁻¹ and melt velocities decreasing from ini-
 753 tially $v_m = 10$ m y⁻¹ to $v_m = 1$ m y⁻¹ at the end of the simulation.

754 Also increasing (`z0p`) or decreasing (`z0m`) the roughness of the ice-ocean interface
 755 by an order of magnitude with respect to the default scenario has a measurable effect
 756 on the development of the plume (Fig. 7b,e,h). As shown by the equilibrium theory (Ap-
 757 pendix B, Fig. B1), an increased roughness should lead to a decreased velocity but to
 758 an increased friction velocity. Since conditions for the equilibrium theory are met for the
 759 later stages of the plume development (Fig. 5a), plume velocity and friction velocity do
 760 show this behaviour here (not shown). With that, higher interfacial roughness leads to
 761 more turbulence inside the plume, and thus a higher entrainment velocity and a higher
 762 melt rate (Figs. 7e,h).

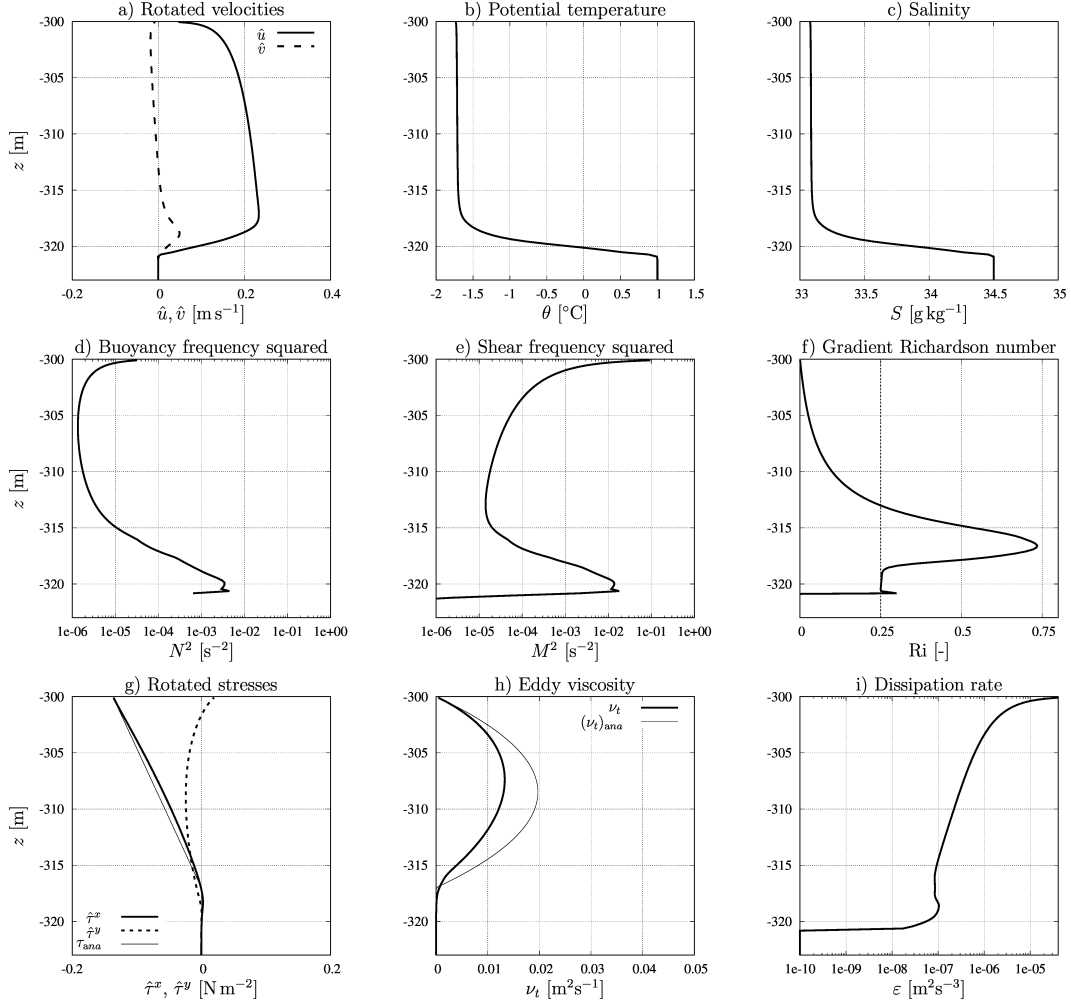


Figure 6. Profiles of a) rotated velocity, b) potential temperature, c) salinity, d) buoyancy frequency squared, e) shear frequency squared, f) gradient Richardson number, g) rotated stresses, h) eddy diffusivity, and i) dissipation rate for the **def** scenario at $t = 14$ days. In panels g) and h) the thin lines show analytical profiles based on the simulated surface stress and a mixed-layer depth diagnosed from the first zero-crossing of the simulated shear stress. In panel f) the dashed line indicates the steady-state Richardson number $Ri_{st} = 0.25$.

763 In contrast, changes in ambient potential temperature (scenarios **tap** and **tam**) have
 764 no significant impact on plume thickness and entrainment velocity (Figs. 7c,f). As ex-
 765 pected, the melt rate increases by about 1.7 m y^{-1} for an increase of 1°C in ambient
 766 temperature (Fig. 7i).

767 **4.2.3 Sensitivity to vertical resolution**

768 To study the effect of coarser vertical resolution in three-dimensional numerical mod-
 769 els, the water column of 150 m height is discretized with $k_{\max} = 50$ layers (10 layers
 770 over the upper 10 m) and $k_{\max} = 25$ layers (5 layers over the upper 10 m) instead of
 771 $k_{\max} = 500$ layers (38 layers over the upper 10 m). Such coarser resolutions are in the
 772 order of what three-dimensional models of ice-cavities using surface-following coordinates
 773 can typically afford. Given the fact that the initial plume thickness of $D = 5 \text{ m}$ is re-

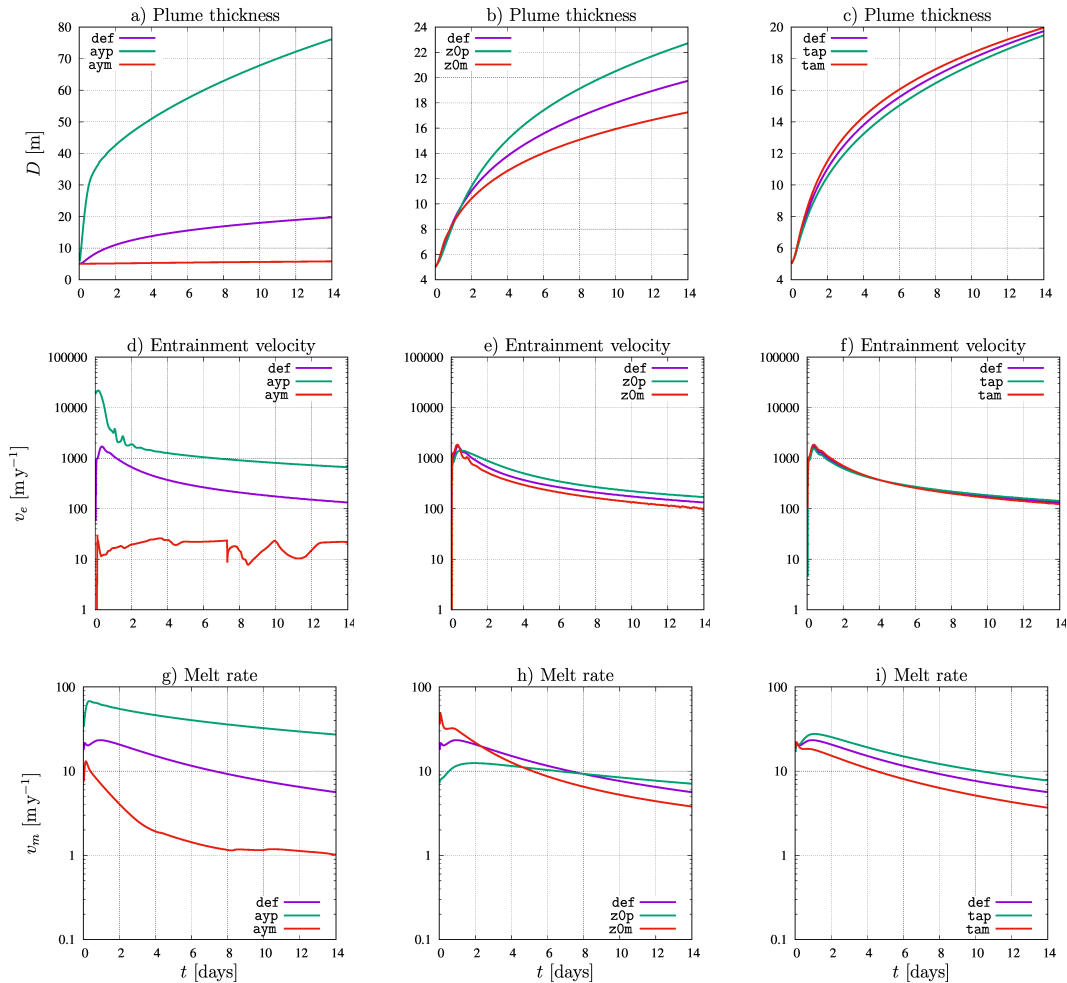


Figure 7. Time series of plume thickness D (panels a, b, c), entrainment velocity v_e (panels d, e, f) and melt rate v_m (panels g, h, i), comparing results of the default scenario **def** with sensitivity simulations **ayp** and **aym** for interfacial slope (panels a, d, g), **z0p** and **z0m** for interfacial roughness (panels b, e, h) and **tap** and **tam** for ambient temperature (panels c, f, i).

774 solved by only a few discrete values, it is already quite coarse. The resulting vertical pro-
 775 files (Fig. 8) for $k_{\max} = 500$, $k_{\max} = 50$ and $k_{\max} = 25$ layers show that the coarse
 776 resolution simulations reproduce the high-resolution profiles with sufficient accuracy. Ve-
 777 locity, potential temperature and salinity profiles (Fig. 8a-c) are reproduced very accu-
 778 rately, due to the largely resolution-independent ocean-to-ice flux parameterization (Sec.
 779 3.1 and 3.2). Buoyancy frequency squared N^2 and shear frequency squared M^2 and thus
 780 the gradient Richardson number (Figs. 8d-f) are well reproduced at the ice-ocean inter-
 781 face and in the plume interior, but at the plume base, the sharp peaks of N^2 and M^2
 782 are not properly resolved. For the coarse resolution with $k_{\max} = 25$ layers, the gradi-
 783 ent Richardson number does not yield a value of $\text{Ri}_{\text{st}} = 0.25$ inside the entrainment layer.

784 Resulting plume thickness, entrainment velocity and melt rate are shown for all three
 785 vertical resolutions in Fig. 9. It can be seen that for $k_{\max} = 50$ layers the development
 786 of the plume thickness is still accurately reproduced with a maximum error of about 1 m
 787 (Fig. 9a). For $k_{\max} = 25$ layers, due to the resolution of the initial plume thickness with
 788 only a few model layers, there is an overall underestimation of the plume thickness by

789 about 3 m, which is however not significantly increasing during the simulation. After some
 790 deviations in the initial phase, also entrainment velocity and melt velocity are well-reproduced
 791 by both coarse resolution simulations (Fig. 9b,c).

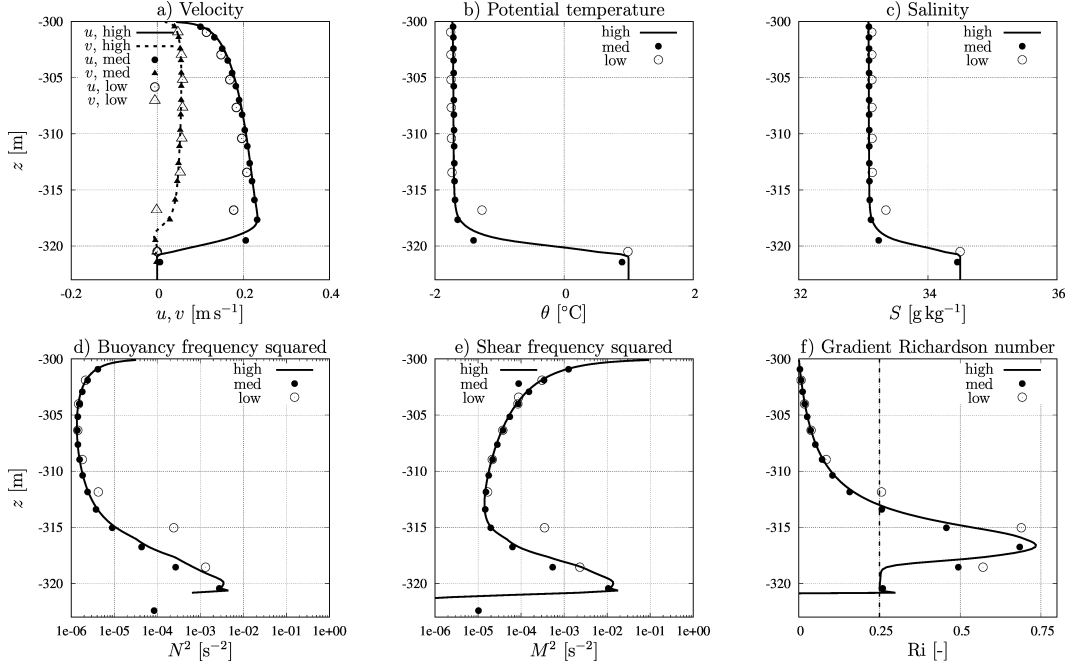


Figure 8. Vertical profiles of a) velocity, b) potential temperature, c) salinity, d) buoyancy frequency squared, e) shear frequency squared and f) gradient Richardson number after 14 days of simulation using the default scenario with high resolution of $k_{\max} = 500$ layers (lines), a medium resolution of $k_{\max} = 50$ layers (black symbols) and a low resolution of $k_{\max} = 25$ layers (open symbols).

792 **4.3 Comparison to entrainment parameterisations**

793 Entrainment is the process of turbulent transport of relatively stagnant ambient
 794 water into the turbulent plume layer through its base with the consequence of an increase
 795 in plume thickness and density. Despite its complex hydrodynamics in a region of sharp
 796 vertical gradients, various parameterizations for the entrainment process have been suc-
 797 cessfully developed. Moreover, computationally efficient vertically integrated models of
 798 subglacial plumes have become a common tool in investigating subglacial melt processes
 799 in ice cavities (Jenkins, 1991; P. R. Holland & Feltham, 2006; Hewitt, 2020). Here, we
 800 first introduce these parameterizations and then compare their performance to the re-
 801 sults of the vertically resolved model for the default scenario and the six sensitivity sce-
 802 narios.

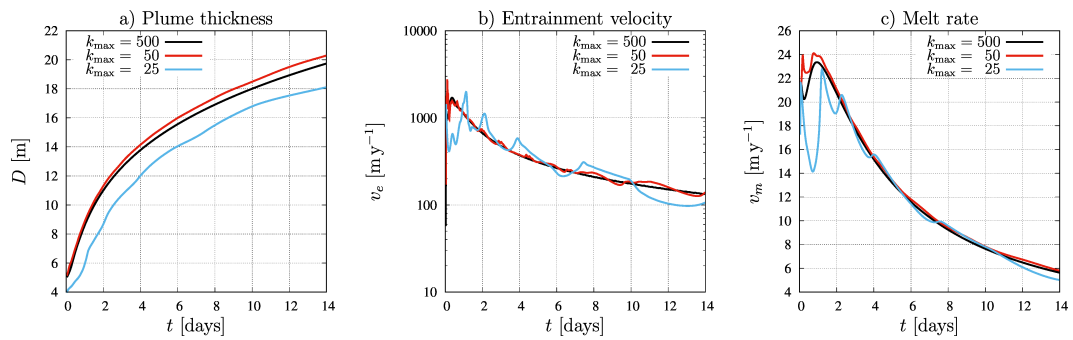


Figure 9. Analysed plume thickness D (panel a), entrainment velocity v_e (panel b) and melt rate v_m (panel c) for the default scenario for three different vertical resolutions during 14 days of simulation. Three different vertical resolutions were applied, $k_{\max} = 500$ layers, $k_{\max} = 40$ layers and $k_{\max} = 20$ layers.

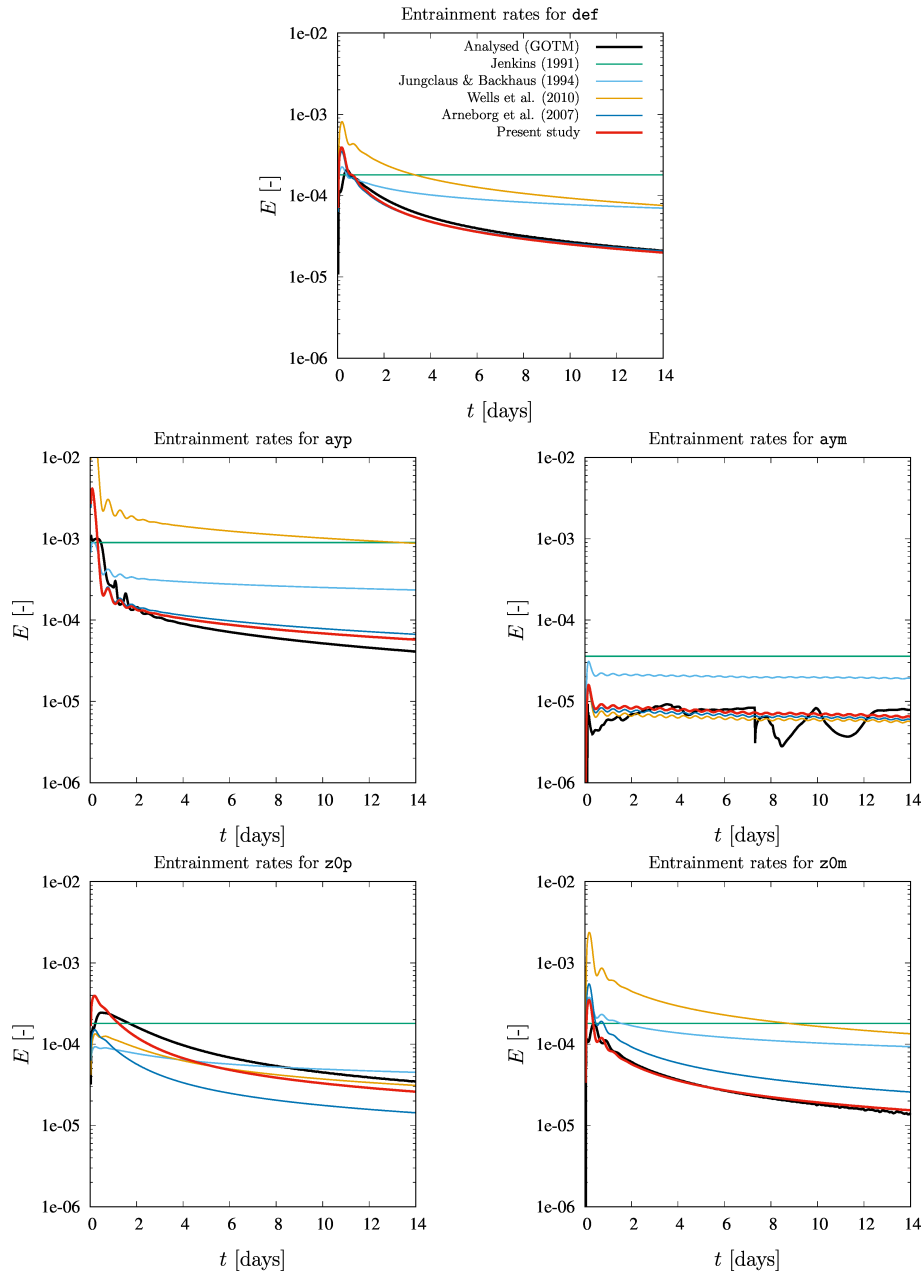


Figure 10. Entrainment rates analysed by GOTM and parameterized by five different entrainment models for the default scenario and the `ayp`, `aym`, `z0p` and `z0m` scenarios. The results for `tap` and `tam` are very similar to those of `def` and are therefore not shown here.

803 The entrainment velocity v_e is defined as the rate of plume thickening due to en-
 804 trainment of ambient water across the plume base. For the parameterisation of the non-
 805 dimensional entrainment rate $E = v_e/\bar{u}_s$, various formulations have been proposed, of
 806 which we are comparing the following five to the vertically resolved entrainment:

- 807 1. A constant entrainment rate has been proposed by Jenkins (1991):

$$808 E = E_0 \sin \alpha \quad (61)$$

809 with $E_0 = 0.036$.

- 810 2. The entrainment model by Jungclaus and Backhaus (1994) calculates the entrain-
 811 ment rate as

$$812 E = \frac{c_L^2}{S_m} \sqrt{1 + \frac{\text{Ri}_b}{S_m}}, \quad (62)$$

813 with the constant empirical parameter $c_L = 0.0275$ and the turbulent Schmidt
 814 number

$$815 S_m = \frac{\text{Ri}_b}{0.725 \left(\text{Ri}_b + 0.186 - \sqrt{\text{Ri}_b^2 - 0.316 \text{Ri}_b + 0.0364} \right)}. \quad (63)$$

816 The present simulations with this modified version showed a substantial under-
 817 estimation of entrainment rates in comparison to other formulations and to the
 818 vertically resolved plume model, such that we retained the original value that Jungclaus
 819 and Backhaus (1994) adopted from Kochergin (1987).

- 820 3. For subcritical flow, Wells et al. (2010) proposed an entrainment rate

$$821 E = \frac{1}{8} \frac{\bar{\Gamma}}{\cos \alpha} \text{Fr}^4 \left(\frac{D}{l_h} \right)^3 \quad (64)$$

822 that depends on the Froude number Fr , with the bulk mixing coefficient $\bar{\Gamma} = 0.2$,
 823 and $0.1 < D/l_h < 0.3$ with the characteristic horizontal turbulent length scale
 824 l_h .

- 825 4. The entrainment rate proposed by Arneborg et al. (2007),

$$826 E = a C_d \text{Fr}^b K^c, \quad (65)$$

827 with $a = 0.084$, $b = 2.65$, $c = 0.6$ and a constant drag coefficient $C_d = 0.0025$
 828 depends on the Ekman number K , additionally.

- 829 5. We finally recalibrate the approach by Arneborg et al. (2007) which has been op-
 830 timized for dense bottom currents in the Baltic Sea using a constant drag coef-
 831 ficient C_d :

$$832 E = \hat{a} c_d \text{Fr}^{\hat{b}} K^{\hat{c}}, \quad (66)$$

833 including now the depth and roughness dependent drag coefficient c_d defined in
 834 (44), using the plume thickness d instead of the upper layer thickness $h_{k_{\max}}$. By
 835 reformulating (66) as

$$836 \ln \left(\frac{E}{c_d} \right) = \ln(\hat{a}) + \hat{b} \ln(\text{Fr}) + \hat{c} \ln(K), \quad (67)$$

837 and formulating the mean-square error between diagnosed and predicted e/c_d as

$$838 f(\hat{a}', \hat{b}, \hat{c}) = \frac{1}{i_{\max}} \sum_{i=1}^{i_{\max}} \left(\hat{a}' + \hat{b} \ln(\text{Fr}_i) + \hat{c} \ln(K_i) - \ln \left(\frac{E_i}{(c_d)_i} \right) \right)^2, \quad (68)$$

839 with $\hat{a}' = \ln(\hat{a})$, where E_i , $(c_d)_i$, Fr_i and K_i are diagnosed values for all exper-
 840 iments and all time steps, a least-square method with $\partial f / \partial \hat{a}' = \partial f / \partial \hat{b} = \partial f / \partial \hat{c} =$
 841 0 gives an optimal parameter set $(\hat{a}, \hat{b}, \hat{c})$ with a minimum error. The resulting val-
 842 ues ($\hat{a} = 0.052$, $\hat{b} = 2.56$ and $\hat{c} = 0.29$) are similar to the original values by

843 Arneborg et al. (2007), but with a significantly smaller influence of the Ekman num-
 844 ber which includes the variable roughness parameter c_d . This model will be de-
 845 noted as *Present study* in Fig. 10.

846 As already shown in Fig. 7, the entrainment velocity can vary over several orders
 847 of magnitude across the different scenarios. In Fig. 10, we compare the non-dimensional
 848 entrainment rates diagnosed from the vertically resolved plume simulations with the val-
 849 ues predicted by the five plume parameterisations given above. The results differ sub-
 850 stantially. For some scenarios, the constant entrainment rate by Jenkins (1991) repro-
 851 duces correctly the order of magnitude of the diagnosed entrainment, but obviously not
 852 its temporal evolution also during later balanced states of the plume. The scenarios in-
 853 cluding variations of the slope angle, \mathbf{a}_{yp} and \mathbf{a}_{ym} , show that the concept of formulat-
 854 ing the entrainment rate as function of the slope angle in this simple parameterization
 855 roughly reproduces the correct order of magnitude of the entrainment process. The bulk
 856 Richardson number dependent parameterisation by Jungclaus and Backhaus (1994) does
 857 largely follow the decreasing trends of the entrainment rate, but is for most scenarios gen-
 858 erally significantly overestimating or underestimating the magnitude, a performance that
 859 is also seen for the parameterization by Wells et al. (2010) which is based on the fourth
 860 power of the Froude number. The performance of the Froude and Ekman number de-
 861 pendent parameterization by Arneborg et al. (2007) is generally better than those pre-
 862 viously discussed, and its accuracy could be strongly improved by the recalibration to
 863 the present seven scenarios. Therefore, the good performance of the original Arneborg
 864 et al. (2007) calibration and the optimal performance of the newly calibrated formula-
 865 tion is not a surprise. This is also because the Arneborg et al. (2007) calibration used
 866 the same turbulence closure model as the present study. But the design of this param-
 867 eterization depending on two non-dimensional plume parameters, Fr and K , that vary
 868 independently (see Fig. 5) seems to be the most promising for rotational plumes.

869 5 Discussion

870 The discussion of the results of this study will concentrate on four issues that might
 871 be of interest for future modeling of ice shelves: the benefits of the analytical solution
 872 (Sec. 5.1), the implications of the numerical analysis (Sec 5.2), the consequences of the
 873 vertical plume structure and resulting entrainment of ambient water (Sec. 5.3) and the
 874 remaining uncertainties in modeling of subglacial plumes and melt rates (Sec. 5.4).

875 5.1 Analytical solution

876 The analytical solution for the vertical profiles of velocity, temperature and salin-
 877 ity of subglacial plumes that is presented as Eqs. (33) - (35) is based on a number of sim-
 878 plifying assumptions: neglect of Earth rotation, vertically homogeneous acceleration of
 879 the plume, parabolic eddy viscosity and diffusivity, and stationarity. Despite its ideal-
 880 ized character, the solution can be used for a number of purposes:

- 881 1. It can be used as a simple test bed for melt flux parameterizations that is not af-
 882 fected by numerical uncertainties. Despite the high degree of simplification, real-
 883 istic values for melt rates and ocean-to-ice heat fluxes were calculated (Sec. 2.5.3).
 884 The analytical solution also shows the high degree of vertical homogeneity of the
 885 profiles of temperature and salinity and the significant differences between bound-
 886 ary and melt-layer values of temperature and salinity, due to the high Schmidt num-
 887 bers (Fig. 2). Also, entrainment fluxes can be quantitatively compared to melt fluxes.
- 888 2. The analytical solution is a basis to construct consistent and convergent formu-
 889 lations for the discrete melt layer fluxes (Sec. 3.1 and 3.2).
- 890 3. Finally, the analytical solution allows for the analysis of numerical convergence
 891 for vertically resolving plume models (Sec. 3.4).

892

5.2 Numerical accuracy

893

894

895

896

897

898

899

900

901

The convergence analysis of a numerical plume model towards the analytical solution (Sec. 3.4) shows that ocean-to-ice fluxes and consequently melt rates can accurately be calculated also with a relatively coarse vertical resolution near the ice-ocean interface. The major requirement to achieve this is the proper discretization of the ocean-to-ice momentum flux. Using a drag coefficient that is independent of the upper-layer thickness leads to highly inaccurate and divergent results, due to the strong velocity gradients near the interface. In contrast, discrete tracer flux formulations that are independent of the upper-layer thickness are numerically inconsistent. Still, they do not lead to a measurable loss of accuracy when the vertical tracer profiles are quasi-homogeneous.

902

903

904

905

906

907

908

909

910

911

912

913

914

915

916

917

918

919

920

921

Vertical resolution does however matter for the numerical reproduction of the entrainment process at the base of the plume, where strong vertical gradients are present. A typical vertical extent of the entrainment layer is of the order of 2 - 4 m (Fig. 6). Although second-moment turbulence closure schemes are relatively robust with respect to vertical resolution (Umlauf & Burchard, 2005; Li et al., 2021), vertical grid resolutions should be of the order of 2 m or higher in the region of the entrainment layer. This is demonstrated in Fig. 8 where an entrainment-layer resolution of about 1.5 m still properly reproduces the vertical plume structure of a high-resolution model at the end of a two-week simulation. Also entrainment velocity and melt rates are sufficiently reproduced by this resolution, but for a resolution of 3 m, results start deteriorating (Fig. 9). For typical plume thicknesses of the order of 10 m, this means that more than 5 numerical layers should be present in the plume region. For geopotential coordinates, this might mean an overall vertical resolution of 2 m at all depths where the ice-ocean interface is present, i.e., typically several 100 m below the undisturbed mean sea level. Also for terrain-following coordinates (where vertical resolution decreases with water depth) such resolutions are still quite a challenge. Here, vertically adaptive coordinates (Hofmeister et al., 2010; Gräwe et al., 2015) may be the solution, since they allow concentrating the resolution at sharp density interfaces such as in the entrainment layer. This principle has been used by Umlauf et al. (2010) for the simulation of channelized dense bottom currents and could also be applied to subglacial plume simulations.

922

5.3 Vertical plume structure and entrainment

923

924

925

926

927

928

929

930

931

932

933

The vertical structure of subglacial plumes is believed to resemble that of dense bottom currents, turned upside down (Jenkins, 2016). That explains why often model tools are applied to subglacial plumes that have been developed for dense bottom currents and oceanic overflows. In both cases, determining entrainment rates is important. For oceanic overflows, the entrainment rates determine their potential for ventilating the deep ocean, for subglacial plumes they determine the transport of relatively warm and salty ambient water towards the ice-ocean interface and therefore play an importance role in setting the melt rate. The fundamental dynamical difference between dense bottom currents and subglacial plumes is the additional (stabilizing) interfacial buoyancy flux due to melt processes at the ice-ocean interface of subglacial plumes that ultimately drives the flow.

934

935

936

937

938

939

940

Entrainment velocities analyzed from the present models results are within the range of common entrainment parameterizations typically used in vertically integrated plume models of subglacial plumes (Fig. 10). Those parameterizations however lead to very different estimates of entrainment rates. To provide a robust and reliable entrainment parameterization, the formulation by Arneborg et al. (2007) has been re-calibrated for a depth-dependent drag coefficient (66) and shows an agreeable accuracy over a large range of plume parameters.

941

5.4 Remaining uncertainties

942

943

944

945

946

947

948

949

950

951

952

953

954

955

The vertical structure of dense bottom currents has been well-observed in the ocean, e.g. the Faroe Bank Channel overflow (Fer et al., 2010) and overflows into the Baltic Sea (Umlauf et al., 2007). Such high-resolution observations of subglacial plumes are not available due to the thickness of the glacial ice cover and the large surface area of the floating ice tongues. The few available observations (e.g., Washam et al., 2020), do not provide sufficient resolution and coverage of the entire plume thickness. It can therefore only be assumed by analogy how subglacial plumes are vertically structured. In agreement with observations and models of dense overflows in the Western Baltic Sea (Arneborg et al., 2007; Umlauf et al., 2007, 2010) with similar characteristics in terms of similarity parameters such as the Froude and Ekman numbers, the interior of subglacial plumes can be assumed to be well-mixed and the plumes can be assumed to be bounded by sharp density interfaces in the entrainment layer. However, the uncertainties about the vertical structure of subglacial plumes can only be reduced by very challenging in-situ field observations under glacial ice tongues.

956

957

958

959

960

961

962

963

964

Moreover, the underlying assumption for one-dimensional water column models of a plume that is laterally homogeneous along the ice-ocean interface is highly idealized and unrealistic. The ice-ocean interface may be smooth on the small scale, but it is plausible to assume non-negligible sub-grid scale roughness that exerts a form drag on the flow. This drag needs to be parameterized in coarse ocean models via an effectively roughness length k_s (Sec. 2.4). Our model experiments show that the roughness length has a large influence on plume thickness, entrainment velocity and melt rate (Fig. 10). Since the determination of this effective roughness is highly uncertain, sensitivity studies with respect to this parameter are recommended.

965

966

967

968

969

970

971

972

973

974

975

The biggest uncertainty however remains for the detailed structure of the topography of the ice-ocean interface and the effects on the plume dynamics. Subglacial plumes are often thought of as wide layers of buoyant water propagating across ice tongues with relatively plain subglacial topographies (P. R. Holland & Feltham, 2006). It is however known that plumes occur as highly channelized flows, similar to overflows in the ocean (Umlauf et al., 2007; Fer et al., 2010), but probably occurring on even smaller scales (Rignot & Steffen, 2008; Washam et al., 2020). To investigate the impact of these topographically highly diverse plume dynamics on the net basal melt rate, detailed studies of more dimensional flows need to be carried out such as cross-sections models of channelized subglacial plumes, similar to the two-dimensional model of dense bottom currents presented by Umlauf et al. (2010).

976

6 Conclusions

977

978

979

980

981

982

983

A numerical one-dimensional water column model of subglacial plumes has been presented here that should help to constrain ocean models of ice shelves. To our knowledge this is the first high-resolution one-dimensional model that couples the physics of the melt layer to second-moment turbulence closures inside the plume and across the entrainment layer. This modeling strategy allows for quantitative predictions of entrainment processes of ambient water into the plume, such that it can serve as a benchmark for models with simpler physics such as bulk entrainment models.

984

985

986

987

988

989

Using an analytical solution of the plume, accurate and convergent numerical expressions for fluxes across the ice-ocean interface are formulated. Specifically, they do also reproduce these fluxes accurately for relatively coarse near-interface resolution. The probably most critical finding is that the vertical model resolution in the region of the entrainment layer should ideally be order of 2 - 3 m, which provides a challenge to existing ocean models for ice shelves. Future efforts should be directed at developing flex-

990 ible numerical schemes that allow this locally high resolution also in large scale ocean
991 models.

992 **Appendix A Derivation of the analytical solution**

993 **A1 Velocity profile**

994 Under the conditions discussed in Sec. 2.1, and ignoring Earth rotation, the mo-
995 mentum budget (7) within the plume has the following form:

$$996 \quad \partial_t u - \partial_{z'} (\nu_t \partial_{z'} u) = b \tan \alpha, \quad (\text{A1})$$

997 with the boundary conditions

$$998 \quad \nu_t \partial_{z'} u = \begin{cases} (u_*^b)^2 & \text{for } z' = 0, \\ u_*^s |u_*^s| & \text{for } z' = D, \end{cases} \quad (\text{A2})$$

999 where u_*^s is the friction velocity in the entrainment layer at the base of the plume. As-
1000 suming stationarity of the velocity profile and combining (A1) and (A2), a linear stress
1001 profile is resulting:

$$1002 \quad \nu_t \partial_{z'} u = (u_*^b)^2 \frac{D - z'}{D} + u_*^s |u_*^s| \frac{z'}{D}. \quad (\text{A3})$$

1003 The parabolic profile of eddy viscosity is given as

$$1004 \quad \nu_t = \kappa u_*^b (z' + z_0) \frac{D - z'}{D}, \quad (\text{A4})$$

1005 see Burchard and Hetland (2010), where for small z' (18) is retained. Combining (A3)
1006 and (A4) gives

$$1007 \quad \partial_{z'} u = \frac{u_*^b}{\kappa} \frac{1}{z' + z_0} + \frac{u_*^s |u_*^s|}{\kappa u_*^b} \frac{z'}{(z' + z_0)(D - z')}. \quad (\text{A5})$$

1008 Integrating (A5) from 0 to z' and using

$$1009 \quad \frac{1}{z' + z_0} + \frac{1}{D - z'} = \frac{D + z_0}{(z' + z_0)(D - z')} \quad (\text{A6})$$

1010 results in

$$1011 \quad u(z') = \frac{u_*^b}{\kappa} \ln \left[\frac{z' + z_0}{z_0} \right] - \frac{u_*^s |u_*^s|}{\kappa u_*^b} \left(\frac{z_0}{D + z_0} \ln \left[\frac{z' + z_0}{z_0} \right] + \frac{D}{D + z_0} \ln \left[\frac{D - z'}{D} \right] \right). \quad (\text{A7})$$

1012 The plume-averaged velocity

$$1013 \quad \bar{u} = \frac{1}{D} \int_0^D u(z') dz', \quad (\text{A8})$$

1014 results from vertical averaging of (A7) as

$$1015 \quad \bar{u} = \frac{u_*^b}{\kappa} A - \frac{u_*^s |u_*^s|}{\kappa u_*^b} \left(\frac{z_0}{D + z_0} A - \frac{D}{D + z_0} \right) \quad (\text{A9})$$

1016 with the integration constant

$$1017 \quad A = \frac{1}{D} \int_0^D \ln \left[\frac{z' + z_0}{z_0} \right] dz' = \frac{D + z_0}{D} \ln \left[\frac{D + z_0}{z_0} \right] - 1. \quad (\text{A10})$$

1018 Combining (A7) and (A9) finally gives the velocity profile fulfilling a prescribed depth-
1019 averaged velocity \bar{u} , see (33).

1020

A2 Tracer profile

1021

Let c be a tracer obeying the following one-dimensional budget equation:

1022

$$\partial_t c + \partial_z f^c = 0, \quad (\text{A11})$$

1023

with the upward turbulent tracer flux,

1024

$$f^c = -\nu'_t \partial_z c = \nu'_t \partial_{z'} c, \quad (\text{A12})$$

1025

the ice-ocean interface value

1026

$$c(z_b - [z_0^c - z_0]) = c_b, \quad (\text{A13})$$

1027

where the location of the boundary value for c at the ice-ocean interface is slightly shifted with respect to the no-slip boundary condition for velocity (see Sec. 2.1, 2.2 and 2.4).

1028

As flux boundary conditions, we define

1030

$$f^c = \begin{cases} f_b^c & \text{for } z' = 0, \\ f_s^c & \text{for } z' = D. \end{cases} \quad (\text{A14})$$

1031

An eddy diffusivity profile is constructed by dividing the parabolic eddy viscosity profile (A4) by the the turbulent Prandtl number Pr_t :

1032

$$\nu'_t = \frac{\kappa}{\text{Pr}_t} |u_*^b| (z' + z_0) \frac{D - z'}{D}, \quad (\text{A15})$$

1033

Assuming that $\partial_t c$ is independent of z , the tracer flux will have the following linear profile:

1034

1035

$$f^c = \nu'_t \partial_{z'} c = f_b^c \frac{D - z'}{D} + f_s^c \frac{z'}{D}. \quad (\text{A16})$$

1036

Combining (A11) and (A16) gives the rate of change of c :

1037

$$\partial_t c = \frac{f_s^c - f_b^c}{D}, \quad (\text{A17})$$

1038

such that the original tracer equation (A11) can be reformulated as

1039

$$\partial_{z'} f^c = -\partial_{z'} f^c = -\frac{f_s^c - f_b^c}{D}. \quad (\text{A18})$$

1040

Combining (A15) and (A16), we obtain

1041

$$\partial_{z'} c = \frac{\text{Pr}_t f_b^c}{\kappa |u_*^b|} (z' + z_0)^{-1} + \frac{\text{Pr}_t f_s^c}{\kappa |u_*^b|} \frac{z'}{(z' + z_0)(D - z')}. \quad (\text{A19})$$

1042

Using (A6) and integrating (A19) from $z_0^c - z_0$ to z' with (A13) reads as

1043

$$\begin{aligned} c(z') - c_b &= \frac{\text{Pr}_t f_b^c}{\kappa |u_*^b|} \ln \left[\frac{z' + z_0}{z_0^c} \right] \\ &\quad - \frac{\text{Pr}_t f_s^c}{\kappa |u_*^b|} \left(\frac{z_0}{D + z_0} \ln \left[\frac{z' + z_0}{z_0^c} \right] + \frac{D}{D + z_0} \ln \left[\frac{D - z'}{D + z_0 - z_0^c} \right] \right) \\ &= \frac{\text{Pr}_t f_b^c}{\kappa |u_*^b|} \left(\ln \left[\frac{z' + z_0}{z_0} \right] + \frac{\kappa}{\text{Pr}_t} \beta^c \right) \\ &\quad - \frac{\text{Pr}_t f_s^c}{\kappa |u_*^b|} \left(\frac{z_0}{D + z_0} \left(\ln \left[\frac{z' + z_0}{z_0} \right] + \frac{\kappa}{\text{Pr}_t} \beta^c \right) \right. \\ &\quad \left. + \frac{D}{D + z_0} \ln \left[\frac{D - z'}{D + z_0 \left(1 - \exp \left[-\frac{\kappa}{\text{Pr}_t} \beta^c \right] \right)} \right] \right) \end{aligned} \quad (\text{A20})$$

1044

1045 with β^c from (31). Vertical averaging of (A20) gives

$$\begin{aligned}
 \bar{c} - c_b &= \frac{\text{Pr}_t f_b^c}{\kappa |u_*^b|} A_c - \frac{\text{Pr}_t f_s^c}{\kappa |u_*^b|} \left(\frac{z_0}{D + z_0} A_c - \frac{D}{D + z_0} \left(1 - \ln \left[\frac{D}{D + z_0 - z_0^c} \right] \right) \right) \\
 &= \frac{\text{Pr}_t f_b^c}{\kappa |u_*^b|} A_c - \frac{\text{Pr}_t f_s^c}{\kappa |u_*^b|} \left(\frac{z_0}{D + z_0} A_c - \right. \\
 &\quad \left. \frac{D}{D + z_0} \left(1 - \ln \left[\frac{D}{D + z_0 \left(1 - \exp \left[-\frac{\kappa}{\text{Pr}_t} \beta^c \right] \right)} \right] \right) \right)
 \end{aligned} \tag{A21}$$

1047 with the vertically averaged tracer concentration \bar{c} and the integration constant

$$\begin{aligned}
 A_c &= \frac{1}{D} \int_0^D \ln \left[\frac{z' + z_0}{z_0^c} \right] dz' = \frac{D + z_0}{D} \ln \left[\frac{D + z_0}{z_0} \right] - \left(1 - \ln \left[\frac{z_0}{z_0^c} \right] \right) \\
 &= \frac{D + z_0}{D} \ln \left[\frac{D + z_0}{z_0} \right] - \left(1 - \frac{\kappa}{\text{Pr}_t} \beta^c \right).
 \end{aligned} \tag{A22}$$

1049 In (A20) - (A22), the formulations including β^c instead of z_0^c , using (30), are those that
 1050 should be used for computations, since z_0^c is typically so small that calculations of its re-
 1051 reciprocal would result in overflows. Combining (A20) and (A21) leads to a tracer profile
 1052 based on the depth mean tracer concentration \bar{c} instead of the melt layer tracer concen-
 1053 tration c_b .

1054 Appendix B Equilibrium dynamics in plume

1055 The depth-averaged bulk dynamics in a well-adjusted plume can approximately be
 1056 described by a steady-state condition for the momentum equations

$$\begin{aligned}
 d_t(\bar{u}D) &= -c_d \bar{u} \bar{u}_s & + \bar{b}D \sin \alpha_x + f \bar{v}D, \\
 d_t(\bar{v}D) &= -c_d \bar{v} \bar{u}_s & + \bar{b}D \sin \alpha_y - f \bar{u}D,
 \end{aligned} \tag{B1}$$

1058 as formulated by (Jenkins, 1991). For a slope aligned with the y -direction ($\alpha_x = 0$) the
 1059 following balance results (Arneborg et al., 2007):

$$\begin{aligned}
 -c_d \bar{u}^{\text{eq}} \left((\bar{u}^{\text{eq}})^2 + (\bar{v}^{\text{eq}})^2 \right)^{1/2} &+ f \bar{v}^{\text{eq}} D = 0, \\
 -c_d \bar{v}^{\text{eq}} \left((\bar{u}^{\text{eq}})^2 + (\bar{v}^{\text{eq}})^2 \right)^{1/2} &+ \bar{b}D \sin \alpha_y - f \bar{u}^{\text{eq}} D = 0,
 \end{aligned} \tag{B2}$$

1061 with the equilibrium velocity vector $(\bar{u}^{\text{eq}}, \bar{v}^{\text{eq}})$. After introducing the non-dimensional
 1062 variables

$$\tilde{u} = \frac{\bar{u}^{\text{eq}}}{fD}; \quad \tilde{v} = \frac{\bar{v}^{\text{eq}}}{fD}; \quad \tilde{u}_s = (\tilde{u}^2 + \tilde{v}^2)^{1/2}; \quad \tilde{b} = \frac{\bar{b}}{f^2 D}; \quad \tilde{u}_*^b = \frac{u_*}{fD} = c_d^{1/2} \tilde{u}_s, \tag{B3}$$

1064 (B2) can be formulated as follows:

$$\begin{aligned}
 -c_d \tilde{u} \tilde{u}_s &= -\tilde{v} \\
 -c_d \tilde{v} \tilde{u}_s + \tilde{b} \sin \alpha_y &= \tilde{u}
 \end{aligned} \tag{B4}$$

1066 Multiplying the first equation in (B4) by \tilde{u} and the second equation by \tilde{v} and subsequently
 1067 adding the results gives

$$-c_d \tilde{u}_s^3 = -\tilde{b} \tilde{v} \sin \alpha_y. \tag{B5}$$

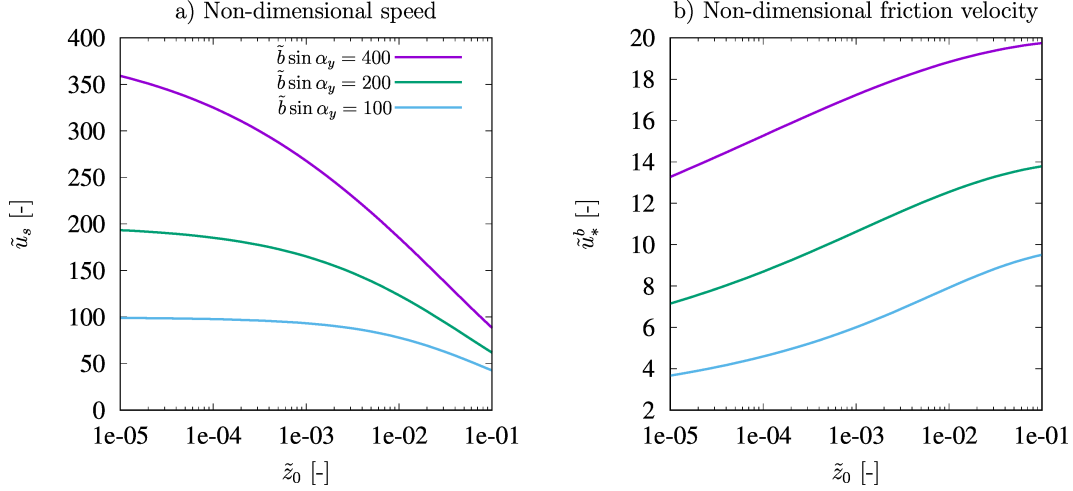


Figure B1. Non-dimensional speed \tilde{u}_s (panel a) and friction velocity \tilde{u}_*^b (panel b) as function of the non-dimensional roughness \tilde{z}_0 for three different values of $\tilde{b} \sin \alpha_y$. For a density difference of $\Delta\rho = 4 \text{ kg m}^{-3}$ between ambient water and plume water, an interfacial slope of $\tan \alpha_y = 10^{-3}$ and a latitude of 79°N , the values $\tilde{b} \sin \alpha_y = (400, 200, 100)$ correspond to plume thicknesses of $D = (25\text{m}, 12.5\text{m}, 6.25\text{m})$.

1069 Multiplying the first equation in (B4) by \tilde{v} and the second equation by \tilde{u} and subsequently
 1070 subtracting the results gives

$$1071 \quad \tilde{u}_s^2 = \tilde{b} \tilde{u} \sin \alpha_y. \quad (\text{B6})$$

1072 Squaring (B5) and (B6), adding the results and rearranging gives

$$1073 \quad \tilde{u}_s^4 + \frac{1}{c_d^2} \tilde{u}_s^2 - \frac{\tilde{b}^2 \sin^2 \alpha_y}{c_d^2} = 0, \quad (\text{B7})$$

1074 which results in

$$1075 \quad \tilde{u}_s^2 = -\frac{1}{2c_d^2} + \sqrt{\frac{1}{4c_d^4} + \frac{\tilde{b}^2 \sin^2 \alpha_y}{c_d^2}} \quad (\text{B8})$$

1076 and consequently

$$1077 \quad (\tilde{u}_*^b)^2 = -\frac{1}{2c_d} + \sqrt{\frac{1}{4c_d^2} + \tilde{b}^2 \sin^2 \alpha_y}. \quad (\text{B9})$$

1078 The velocity components \tilde{u} and \tilde{v} can be calculated by means of (B5) and (B6).

1079 The dependence of the non-dimensional current speed \tilde{u}_s and the non-dimensional
 1080 friction velocity $\tilde{u}_*^b = c_d^{1/2} \tilde{u}_s$ on the non-dimensional interfacial roughness is shown in
 1081 Fig. B1 for three different values of the non-dimensional buoyancy forcing $\tilde{b} \sin \alpha_y$. Ex-
 1082 pectedly, a larger roughness length leads to an decreased plume velocity, however, it leads
 1083 to an increased friction velocity indicating a more turbulent plume. This can be explained
 1084 by the fact that the decrease of current speed due to increased roughness \tilde{z}_0 is smaller
 1085 than the corresponding increase in $c_d^{1/2}$. This non-linear effect is not reproduced by mod-
 1086 els that use a constant drag coefficient.

1087 Acknowledgments

1088 The work of this study has been supported by the collaborative project GROCE (Green-
 1089 land Ice Sheet Ocean Interaction) funded by the German Federal Ministry of Research

1090 and Education under the grant no. 03F0855E. The implementation of the additional sub-
 1091 glacial plume processes has been financially supported by the Leibniz Institute of Baltic
 1092 Sea Research Warnemünde through a contract with Bolding & Bruggeman ApS in Den-
 1093 mark. Much of the work for this study by Hans Burchard have been carried out during
 1094 a sabbatical visit at the Scottish Association of Marine Science in Oban (Scotland). The
 1095 authors are grateful for the constructive comments by Knut Klingbeil (Warnemünde, Ger-
 1096 many) on earlier versions of the manuscript.

1097 Software Availability Statement: The source on which this study is based can be
 1098 accessed here: <https://github.com/gotm-model/code/tree/plume>. The ice module can
 1099 be found here:
 1100 https://github.com/BoldingBruggeman/stim/tree/bafl/src/models/basal_melt. Setup
 1101 and output for the default scenario are provided at
 1102 <https://github.com/gotm-model/cases/tree/master/plume>. Note to reviewers of this sub-
 1103 mission: For the final manuscript version, a link to zenodo will be provided instead.

1104 References

- 1105 Absi, R. (2021). Reinvestigating the parabolic-shaped eddy viscosity profile for free
 1106 surface flows. *Hydrology*, *8*(3), 126.
- 1107 Arneborg, L., Fiekas, V., Umlauf, L., & Burchard, H. (2007). Gravity current
 1108 dynamics and entrainment - A process study based on observations in the
 1109 Arkona Basin. *J. Phys. Oceanogr.*, *37*(8), 2094–2113.
- 1110 Burchard, H., & Baumert, H. (1995). On the performance of a mixed-layer model
 1111 based on the κ - ϵ turbulence closure. *J. Geophys. Res.*, *100*(C5), 8523–8540.
- 1112 Burchard, H., & Bolding, K. (2001). Comparative analysis of four second-moment
 1113 turbulence closure models for the oceanic mixed layer. *J. Phys. Oceanogr.*,
 1114 *31*(8), 1943–1968.
- 1115 Burchard, H., & Hetland, R. D. (2010). Quantifying the contributions of tidal
 1116 straining and gravitational circulation to residual circulation in periodically
 1117 stratified tidal estuaries. *J. Phys. Oceanogr.*, *40*, 1243–1262.
- 1118 Burchard, H., & Petersen, O. (1999). Models of turbulence in the marine environ-
 1119 ment - A comparative study of two-equation turbulence models. *J. Mar. Syst.*,
 1120 *21*(1-4), 29–53.
- 1121 Burchard, H., Schuttelaars, H. M., & Geyer, W. R. (2013). Residual sediment
 1122 fluxes in weakly-to-periodically stratified estuaries and tidal inlets. *J. Phys.*
 1123 *Oceanogr.*, *43*(9), 1841–1861.
- 1124 Cheng, C., Jenkins, A., Wang, Z., & Liu, C. (2020). Modeling the vertical structure
 1125 of the ice shelf–ocean boundary current under supercooled condition with sus-
 1126 pended frazil ice processes: A case study underneath the Amery Ice Shelf, East
 1127 Antarctica. *Ocean Modell.*, *156*, 101712.
- 1128 Cheng, Y., Canuto, V., & Howard, A. (2002). An improved model for the turbulent
 1129 pbl. *J. Atmos. Sci.*, *59*(9), 1550–1565.
- 1130 Church, J. A., White, N. J., Konikow, L. F., Domingues, C. M., Cogley, J. G., Rig-
 1131 not, E., ... Velicogna, I. (2011). Revisiting the Earth’s sea-level and energy
 1132 budgets from 1961 to 2008. *Geophys. Res. Lett.*, *38*(18).
- 1133 Dansereau, V., Heimbach, P., & Losch, M. (2014). Simulation of subice shelf melt
 1134 rates in a general circulation model: Velocity-dependent transfer and the role
 1135 of friction. *J. Geophys. Res.*, *119*(3), 1765–1790.
- 1136 Dinniman, M. S., Klinck, J. M., & Smith Jr, W. O. (2007). Influence of sea ice
 1137 cover and icebergs on circulation and water mass formation in a numerical
 1138 circulation model of the Ross Sea, Antarctica. *J. Geophys. Res.*, *112*(C11).
- 1139 Fer, I., Voet, G., Seim, K. S., Rudels, B., & Latarius, K. (2010). Intense mixing of
 1140 the Faroe Bank Channel overflow. *Geophys. Res. Lett.*, *37*(2).
- 1141 Goldberg, D., Holland, D. M., & Schoof, C. (2009). Grounding line movement

- 1142 and ice shelf buttressing in marine ice sheets. *J. Geophys. Res.*, *114*, F04026,
1143 doi:10.1029/2008JF001227.
- 1144 Gräwe, U., Holtermann, P., Klingbeil, K., & Burchard, H. (2015). Advantages of
1145 vertically adaptive coordinates in numerical models of stratified shelf seas.
1146 *Ocean Modell.*, *92*, 56–68.
- 1147 Gwyther, D. E., Kushara, K., Asay-Davis, X. S., Dinniman, M. S., & Galton-Fenzi,
1148 B. K. (2020). Vertical processes and resolution impact ice shelf basal melting:
1149 A multi-model study. *Ocean Modell.*, *147*, 101569.
- 1150 Haney, R. L. (1991). On the pressure gradient force over steep topography in sigma
1151 coordinate ocean models. *J. Phys. Oceanogr.*, *21*(4), 610–619.
- 1152 Hellmer, H. H., & Olbers, D. J. (1989). A two-dimensional model for the thermoha-
1153 line circulation under an ice shelf. *Antarctic Sci.*, *1*(4), 325–336.
- 1154 Hewitt, I. J. (2020). Subglacial plumes. *Ann. Rev. Fluid Mech.*, *52*, 145–169.
- 1155 Hofmeister, R., Burchard, H., & Beckers, J.-M. (2010). Non-uniform adaptive verti-
1156 cal grids for 3D numerical ocean models. *Ocean Modell.*, *33*(1-2), 70–86.
- 1157 Holland, D. M., & Jenkins, A. (1999). Modeling thermodynamic ice–ocean interac-
1158 tions at the base of an ice shelf. *J. Phys. Oceanogr.*, *29*(8), 1787–1800.
- 1159 Holland, P. R., & Feltham, D. L. (2006). The effects of rotation and ice shelf topog-
1160 raphy on frazil-laden ice shelf water plumes. *J. Phys. Oceanogr.*, *36*(12), 2312–
1161 2327.
- 1162 Jackett, D. R., McDougall, T. J., Feistel, R., Wright, D. G., & Griffies, S. M. (2006).
1163 Algorithms for density, potential temperature, conservative temperature, and
1164 the freezing temperature of seawater. *J. Atmos. Ocean. Tech.*, *23*(12), 1709–
1165 1728.
- 1166 Jenkins, A. (1991). A one-dimensional model of ice shelf–ocean interaction. *J. Geo-
1167 phys. Res.*, *96*(C11), 20671–20677.
- 1168 Jenkins, A. (1992). *Dynamics of Ronne ice shelf and its interaction with the ocean*
1169 (Unpublished doctoral dissertation). British Antarctic Survey, Natural Envi-
1170 ronment Research Council, Cambridge, England.
- 1171 Jenkins, A. (2011). Convection-driven melting near the grounding lines of ice shelves
1172 and tidewater glaciers. *J. Phys. Oceanogr.*, *41*(12), 2279–2294.
- 1173 Jenkins, A. (2016). A simple model of the ice shelf–ocean boundary layer and cur-
1174 rent. *J. Phys. Oceanogr.*, *46*(6), 1785–1803.
- 1175 Jenkins, A. (2021). Shear, stability, and mixing within the ice shelf–ocean boundary
1176 current. *J. Phys. Oceanogr.*, *51*(7), 2129–2148.
- 1177 Jenkins, A., Hellmer, H. H., & Holland, D. M. (2001). The role of meltwater ad-
1178 vection in the formulation of conservative boundary conditions at an ice–ocean
1179 interface. *J. Phys. Oceanogr.*, *31*(1), 285–296.
- 1180 Jenkins, A., Nicholls, K. W., & Corr, H. F. (2010). Observation and parameteriza-
1181 tion of ablation at the base of Ronne Ice Shelf, Antarctica. *J. Phys. Oceanogr.*,
1182 *40*(10), 2298–2312.
- 1183 Jungclauss, J. H., & Backhaus, J. O. (1994). Application of a transient reduced grav-
1184 ity plume model to the Denmark Strait Overflow. *J. Geophys. Res.*, *99*(C6),
1185 12375–12396.
- 1186 Kader, B. A. (1981). Temperature and concentration profiles in fully turbulent
1187 boundary layers. *Int. J. Heat Mass Transfer*, *24*(9), 1541–1544.
- 1188 Kader, B. A., & Yaglom, A. M. (1972). Heat and mass transfer laws for fully turbu-
1189 lent wall flows. *Int. J. Heat Mass Transfer*, *15*(12), 2329–2351.
- 1190 Klingbeil, K., Lemarié, F., Debreu, L., & Burchard, H. (2018). The numerics of
1191 hydrostatic structured-grid coastal ocean models: State of the art and future
1192 perspectives. *Ocean Modell.*, *125*, 80–105.
- 1193 Kochergin, V. P. (1987). Three-dimensional prognostic models. In N. S. Heaps (Ed.),
1194 *Three-dimensional coastal ocean models* (Vol. 4, pp. 201–208). Wiley Online Li-
1195 brary.
- 1196 Lange, X., & Burchard, H. (2019). The relative importance of wind straining and

- 1197 gravitational forcing in driving exchange flows in tidally energetic estuaries. *J.*
1198 *Phys. Oceanogr.*, *49*(3), 723–736.
- 1199 Li, Q., Bruggeman, J., Burchard, H., Klingbeil, K., Umlauf, L., & Bolding, K.
1200 (2021). Integrating CVMix into GOTM (v6. 0): A consistent framework
1201 for testing, comparing, and applying ocean mixing schemes. *Geosci. Model*
1202 *Dev.*, *14*, 4261–4282.
- 1203 Losch, M. (2008). Modeling ice shelf cavities in a z coordinate ocean general circulation
1204 model. *J. Geophys. Res.*, *113*, C08043, doi:10.1029/2007JC004368.
- 1205 Mayer, C., Schaffer, J., Hattermann, T., Floricioiu, D., Krieger, L., Dodd, P. A.,
1206 ... Schannwell, C. (2018). Large ice loss variability at Nioghalvfjærdsfjorden
1207 glacier, northeast-greenland. *Nature*, *9*(1), 1–11.
- 1208 Mellor, G. L., McPhee, M. G., & Steele, M. (1986). Ice-seawater turbulent boundary
1209 layer interaction with melting or freezing. *J. Phys. Oceanogr.*, *16*(11), 1829–
1210 1846.
- 1211 Münchow, A., Padman, L., & Fricker, H. A. (2014). Interannual changes of the float-
1212 ing ice shelf of Petermann Gletscher, North Greenland, from 2000 to 2012. *J.*
1213 *Glaciol.*, *60*(221), 489–499.
- 1214 Omstedt, A., & Svensson, U. (1984). Modeling supercooling and ice formation in a
1215 turbulent Ekman layer. *J. Geophys. Res.*, *89*(C1), 735–744.
- 1216 Payne, A. J., Holland, P. R., Shepherd, A. P., Rutt, I. C., Jenkins, A., & Joughin, I.
1217 (2007). Numerical modeling of ocean-ice interactions under Pine Island Bay’s
1218 ice shelf. *J. Geophys. Res.*, *112*(C10).
- 1219 Rignot, E., & Steffen, K. (2008). Channelized bottom melting and stability of float-
1220 ing ice shelves. *Geophys. Res. Lett.*, *35*(2).
- 1221 Rosevear, M. G., Gayen, B., & Galton-Fenzi, B. K. (2021). The role of double-
1222 diffusive convection in basal melting of antarctic ice shelves. *Proc. Nat. Acad.*
1223 *Sci.*, *118*(6).
- 1224 Schaffer, J., Kanzow, T., von Appen, W.-J., von Albedyll, L., Arndt, J. E., &
1225 Roberts, D. H. (2020). Bathymetry constrains ocean heat supply to Green-
1226 land’s largest glacier tongue. *Nature Geosci.*, *13*(3), 227–231.
- 1227 Steele, M., Mellor, G. L., & McPhee, M. G. (1989). Role of the molecular sublayer in
1228 the melting or freezing of sea ice. *J. Phys. Oceanogr.*, *19*(1), 139–147.
- 1229 Straneo, F., & Cenedese, C. (2015). The dynamics of Greenland’s glacial fjords and
1230 their role in climate. *Annu. Rev. Mar. Sci.*, *7*, 89–112.
- 1231 Timmermann, R., Wang, Q., & Hellmer, H. (2012). Ice-shelf basal melting in a
1232 global finite-element sea-ice/ice-shelf/ocean model. *Annals Glaciology*, *53*(60),
1233 303–314.
- 1234 Umlauf, L. (2009). The description of mixing in stratified layers without shear in
1235 large-scale ocean models. *J. Phys. Oceanogr.*, *39*(11), 3032–3039.
- 1236 Umlauf, L., & Arneborg, L. (2009). Dynamics of rotating shallow gravity currents
1237 passing through a channel. part i: Observation of transverse structure. *J.*
1238 *Phys. Oceanogr.*, *39*(10), 2385–2401.
- 1239 Umlauf, L., Arneborg, L., Burchard, H., Fiekas, V., Lass, H., Mohrholz, V., &
1240 Prandke, H. (2007). Transverse structure of turbulence in a rotating grav-
1241 ity current. *Geophys. Res. Lett.*, *34*(8).
- 1242 Umlauf, L., Arneborg, L., Hofmeister, R., & Burchard, H. (2010). Entrainment
1243 in shallow rotating gravity currents: A modeling study. *J. Phys. Oceanogr.*,
1244 *40*(8), 1819–1834.
- 1245 Umlauf, L., & Burchard, H. (2005). Second-order turbulence closure models for geo-
1246 physical boundary layers. A review of recent work. *Conti. Shelf Res.*, *25*(7-8),
1247 795–827.
- 1248 Vreugdenhil, C. A., & Taylor, J. R. (2019). Stratification effects in the turbulent
1249 boundary layer beneath a melting ice shelf: Insights from resolved large-eddy
1250 simulations. *J. Phys. Oceanogr.*, *49*(7), 1905–1925.
- 1251 Washam, P., Nicholls, K. W., Münchow, A., & Padman, L. (2020). Tidal modula-

- 1252 tion of buoyant flow and basal melt beneath Petermann Gletscher Ice Shelf,
1253 Greenland. *J. Geophys. Res.*, *125*(10), e2020JC016427.
- 1254 Wells, M., Cenedese, C., & Caulfield, C. (2010). The relationship between flux co-
1255 efficient and entrainment ratio in density currents. *J. Phys. Oceanogr.*, *40*(12),
1256 2713–2727.
- 1257 Yaglom, A. M., & Kader, B. A. (1974). Heat and mass transfer between a rough
1258 wall and turbulent fluid flow at high Reynolds and Peclet numbers. *J. Fluid*
1259 *Mech.*, *62*(3), 601-623.